

1 Impact of the Madden Julian Oscillation on the summer West
2 African monsoon in AMIP simulations.

3 Coumba NIAN ^{1, 2, 3, 4*}, Elsa Mohino ³, Amadou T. Gaye ¹, J. Bayo Omotosho ⁴

4 ¹Laboratoire de Physique de l'Atmosphere et de l'Ocean Simeon Fongang (LPAO-SF), ESP,
5 Dakar, Senegal
6 Ecole Superieure Polytechnique - Universite Cheikh Anta Diop, Dakar
7 BP 5085 Dakar-Fann, Dakar, Senegal

8
9 ² Instituto de Geociencias (IGEO), Agencia Estatal Consejo Superior de Investigaciones Cien-
10 tificas CSIC, Madrid, Spain

11
12 ³ Departamento de Fisica de la Tierra, Astronomia y Astrofisica I, Geofisica y Meteorolo-
13 gia, Universidad Complutense de Madrid (UCM), Madrid, Spain

14
15 ⁴ WASCAL, Department of Meteorology, Federal University of Technology Akure (Nigeria)

16
17 Corresponding author address : Coumba NIAN, Universidad Complutense de Madrid Facul-
18 tad de Fisicas Departamento de Meteorologia, 28040 Madrid, Tel : (0034)913944440.

19 Email : niangcoumba@hotmail.fr

Abstract

At intraseasonal timescales, convection over West Africa is modulated by the Madden Julian Oscillation (MJO). In this work we investigate the simulation of such relationship by 11 state-of-the-art Atmospheric General Circulation Models run with prescribed observed Sea Surface Temperatures (SST). In general, the Atmospheric Model Intercomparison Project (AMIP) simulations show good skill in capturing the main characteristics of the summer MJO as well as its influence on convection and rainfall over West Africa. Most models simulate an eastward spatiotemporal propagation of enhanced and suppressed convection similar to the observed MJO, although their signal over West Africa is weaker in some models. In addition, the ensemble average of models gives a better performance in reproducing the main features and timing of the MJO and its impact over West Africa. The influence on rainfall is well captured in both Sahel and Guinea regions thereby adequately producing the transition between positive and negative rainfall anomalies through the different phases as in the observation. Furthermore, the results show that a strong active convection phase is clearly associated with a stronger African Easterly Jet (AEJ) but the weak convective phase is associated with a much weaker AEJ. Our analysis of the equatorial waves suggests that the main impact over West Africa is established by the propagation of low-frequency waves within the MJO and Rossby spectral peaks. Results from the simulations confirm that it may be possible to predict anomalous convection over West Africa with a time lead of 15-20 day.

Keywords : Madden Julian Oscillation, summer rainfall, West Africa, AMIP simulations.

1. Introduction

The madden Julian Oscillation is a tropical disturbance that propagates eastward around the tropics from the western Indian Ocean to the western Pacific Ocean with a periodicity of around 30-90 days (Madden et al. 1971). This phenomenon was firstly identified by Madden and Julian (1971) by analysing zonal wind anomalies data from Canton Island. It is a large scale coupling between the atmospheric circulation and the tropical deep convection (Zhang 2005). Madden and Julian (1994) describe the MJO as the most dominant mode of intraseasonal variability over the tropical atmosphere. It has been estimated that one-half of tropical

49 intraseasonal variance over the western Pacific is explained by the MJO (Hendon et al. 1999 ;
50 Kessler 2001).

51 The MJO has a wide range of impacts, affecting precipitation and atmospheric circulation
52 around the tropics and subtropics (Yasunari 1979 ; Wheeler and McBride 2005 ; Zhang 2005 ;
53 Donald et al. 2006). It also influences tropical cyclone activity in the eastern Pacific and At-
54 lantic basins during the Northern Hemisphere summer (Liebmann et al. 1994 ; Maloney and
55 Hartmann 2000b ; Ventrice et al. 2011). Furthermore, some studies have also highlighted a
56 relationship between the MJO signal and heavy precipitation events over California, South
57 Atlantic, Southwest Asia and also East Africa (Higgins et al. 2000 ; Jones et al. 2000 ; Bond
58 and Vecchi 2003 ; Carvalho et al. 2004 ; Liebmann et al. 2004a ; Wheeler and Hendon 2004 ;
59 Barlow et al. 2005).

60 The economy of West African countries is highly dependent on agricultural and water re-
61 sources, which makes them highly vulnerable to rainfall variability, especially at intraseasonal
62 time scales (Gadgil and Rao 2000 ; Sultan et al. 2005). The occurrence of wet and dry spells
63 can significantly modulate the crop yield, which is a function of the repartition of rainfall
64 during the season (Janicot and Sultan 2001). At these time scales, there are two main modes
65 of variability over West Africa at 10-25 days and 25-60 days (Janicot and Sultan 2001 ; Sultan
66 et al. 2003 ; Mounier et al. 2004 ; Mounier et al. 2007). Rainfall variability in the 25-60
67 day range appears to have a MJO contribution since they share the same range of periodicity.
68 Despite some works that suggested a weak or non-existence relation between the MJO and
69 anomalous convection over West Africa (Knutson and Weickmann 1987 ; Maloney and Hart-
70 mann 2000a), more recent studies point to a 20 days lag between enhanced convection over the
71 Indian Ocean associated with the MJO and reduced convection over West Africa (Matthews
72 2004 ; Maloney and Shaman 2008 ; Janicot et al. 2009 ; Lavender and Matthews 2009 ; Pohl et
73 al. 2009 ; Mohino et al. 2012).

74 Despite all the studies performed, the mechanisms through which MJO impacts West Africa
75 is not clearly understood. Matthews (2004) and Maloney and Shaman (2008) suggest that
76 eastward dry equatorial Kelvin and westward Rossby equatorial waves triggered by MJO ac-
77 tivity over the warm pool can explain the impact of the MJO on West Africa. Lavender and
78 Matthews (2009) show that locally reduced convection associated with latent heating anoma-
79 lies over the warm pool that force dry equatorial westward Rossby and eastward Kelvin waves

reach Africa approximately 20 days later. The studies of Janicot et al. (2009) and Mohino et al. (2012) highlight the role of convectively coupled Rossby waves in explaining the overall impact of the MJO on convection anomalies over West Africa.

GCMs still have problems to realistically represent the MJO signal (Slingo et al. 1996 ; Waliser et al. 2003 ; Lin et al. 2006 ; Zhang et al. 2006 ; Kim et al. 2009). The spectral analysis in the 30-70 day periodicity of 200 hPa velocity potential from atmosphere-only GCM simulations shows the inability of models to properly simulate the observed spectral peak in the zonal wavenumber 1 (Slingo et al. 1996). In addition, Lin et al. (2006) examined Coupled Model Intercomparison Project phase 3 (CMIP3) models and found that only two models simulated a realistic variance and the main features of the MJO rainfall pattern. From the set of GCM models analysed by Kim et al. (2009) only two showed relatively better skill in representing the MJO. Recently, Hung et al. (2013) evaluated the MJO and convectively coupled equatorial waves using simulations from the Coupled Models Intercomparison Project phase 5 (CMIP5). Their results show that the CMIP5 models exhibit an overall improvement with respect to CMIP3 in simulating the tropical intraseasonal variability of rainfall with larger MJO variance. Crueger et al. (2013) performed a variety of uncoupled (AMIP-style) and coupled simulations with different grid resolutions. Their analysis suggests that atmosphere-only experiments show less MJO variability than coupled models (typically one-quarter and one-third of the variance found in reanalysis, respectively). However, they concluded that the air-sea coupling is not the most relevant factor for a good MJO simulation. In fact, Mauritsen et al. (2012) show that a robust MJO simulation is mainly related to the ability of a GCM to represent the moisture-stratiform instability process, low-level moisture convergence and discharge-recharge mechanism. Despite the numerous works devoted to the assessment of MJO simulation in coupled and uncoupled models, very few have evaluated the simulation of the MJO impact over West Africa. Such an evaluation can help improve our understanding of the mechanisms underlying the MJO-West Africa link and are also a first step to know if middle-range dynamical prediction of dry and wet spells over West Africa is feasible.

The aim of this paper is to evaluate the simulation of the impact of the MJO on rainfall and convection over West Africa and the dynamical mechanism involved in state-of-the-art models. For this aim, we use a set of AMIP simulations from models participating in CMIP5.

2. Data and Methodology

2.1 Data

2.1.1 Observational datasets

Daily interpolated Outgoing Longwave Radiation (OLR) measured from National Oceanic and Atmospheric Administration (NOAA) is used as indicator of convection (Liebmann and Smith 1996) in the tropical region. It spans the period from mid-1974 to present and it has a horizontal resolution of 2.5° . The daily global rainfall data with a spatial resolution of 1° used in this study comes from GPCP data set and covers the period from 1997 to present (Huffman et al. 2001). For zonal winds, we use reanalysis data from ERA-40 (Uppala et al. 2005) and ERA-Interim (Dee and Uppala 2009) to study the dynamics associated with the MJO. The former is used from 2001 to 2008 while the latter is used for the 1979-2000 period. All datasets used through the study are interpolated into a grid of 3° in longitude and 2° in latitude for a better comparison among all simulations. In this study we focus on the extended summer season which is calculated from 1st May to 30th September in the period 1979-2008.

2.1.2 Model simulations

In this study we use simulations carried out in the framework of the CMIP5 (Taylor et al. 2012) project. Among all the simulations, we focus on the AMIP experiment, which were performed by Atmosphere General Circulation Models, forced with prescribed SST variations in the 1979-present period. The basic purpose of AMIP simulations is to pledge the systematic intercomparison and validation of the performance of GCMs on intraseasonal timescale as well as to perform some models diagnostic under realistic conditions (Taylor et al. 2012). An overview of the models with the ensemble members, convection schemes and horizontal resolutions of the simulations is provided in Table 1. The number of ensembles used differs from one model to another based on the availability of data. For each model daily outgoing longwave radiation and zonal winds at 200 and 850hPa are used to define the MJO index and also to study the dynamics related to it. The simulated rainfall is also used to estimate the impact of the MJO on West African rainfall variability.

2.2 Methodology

2.2.1 Definition of the MJO cycle in observations

For this study the MJO cycle is analyzed using an approach similar to the one proposed by Wheeler and Hendon (2004). We firstly apply a 20-90 day band-pass filter to extract the periodicity related to the MJO signal, while removing as well the annual cycle and the interannual variability. Then standardized anomalies of zonal winds and OLR are computed and averaged over the tropics between 15°S - 15°N . A Combined Empirical Orthogonal Function (CEOF) analysis (Venegas 2001) is performed on the zonal winds at 850 and 200hPa and OLR. The two leading CEOF modes are used to describe the MJO activity and to build composite maps that illustrate the progression of the MJO along the equator with a succession of enhanced and suppressed convection events. A two-dimensional phase diagram is built with the Principal Components (PCs) of the two leading CEOFs. Such phase diagram is further divided into eight sectors corresponding to the eight phases with which we describe the MJO cycle (Fig. 1d). Each phase of the cycle is estimated as a composite map using all the dates that lie in the same sector of the phase diagram. Only those dates in which the MJO index exceeds a threshold of one standard deviation are used to build the composite maps. A two-tailed t-test is applied to evaluate the statistical significance of the composite maps.

To estimate the time it takes for the MJO to cover its cycle we first track the MJO evolution in the phase space and define an MJO event when at least 4 complete consecutive phases are covered by its evolution. We then divide the total number of days taken by that event by the number of complete phases crossed and we average over all events in all years and obtain the average time it takes for the MJO to cover a phase of its cycle.

2.2.2 Definition of the MJO cycle in simulations

For the simulations, the same procedure is followed to obtain the CEOF modes : we apply the same 20-90 day band-pass filter and we standardize anomalies and average them in the 15°S - 15°N region. The anomalies from those models with ensemble runs are concatenated in time before the CEOF analysis. The two leading CEOF modes can also be used to describe the simulated MJO cycle (as it is shown in section 3). However, for most models the CEOF patterns obtained are shifted with respect to the observations. In Fig. 1, we show an example

168 for the CNRM-CM5 model : the CEOF patterns for the zonal wind at 850hPa of the two
 169 leading modes shows a structure similar to the one obtained from observations though shifted
 170 to the west (Figs. 1a, 1b). The model's results for the CEOF patterns of OLR and zonal
 171 wind at 200hPa are consistent with this westward shift (not shown). Since the MJO patterns
 172 propagate eastwards, this means that the CNRM-CM5 CEOF patterns lag the observed ones.
 173 In order to better compare the CEOF patterns among models and with the observations, we
 174 shift the modelled ones in longitude towards the observed ones. To choose the best angle for
 175 the shift, we perform a lead-lag correlation in longitude between the observed CEOF patterns
 176 and the modelled ones (Fig. 1c). Note that all six CEOF patterns (three variables times two
 177 CEOF modes) are concatenated together for this calculation. The longitude angle that maxi-
 178 mizes the correlation is chosen to shift all CEOF patterns (Fig. 1a, 1b, dashed red curve). The
 179 shift angles differ from one model to another (Fig. 1f).
 180 As with the observations, the Principal Components of the two leading CEOFs in each model
 181 are used to build a two-dimensional diagram. However, for those models that show a shift
 182 between their CEOF patterns and the observed ones, the definition of the MJO cycle based
 183 on dividing the PC phase space in the same 8 sectors as in observations (Fig. 1d) leads to a
 184 shift in the modelled MJO cycle with respect to the observed ones. This is expected since those
 185 dates in the models when PC1 (PC2) are strong, show anomalies mostly related to CEOF1
 186 (CEO2) in the models, which are shifted in longitude with respect to observations.
 187 The composite approach we use for observations assumes an ideal MJO cycle, in which ano-
 188 malies propagate eastward as the MJO describes a circumference in the phase space travelling
 189 anticlockwise. In such a model, the MJO anomalies go round the planet (propagate 360° east
 190 in longitude until they return back to the origin) in the time it takes to go 360° round the
 191 phase space. If we suppose a uniform speed for the MJO anomalies to travel the cycle, a shift
 192 of α in longitude can be directly translated to a shift in α in the phase space. With this in
 193 mind and in order to better compare the MJO cycle among models and with the observations,
 194 we divide the phase space for the models into 8 sectors that are shifted with respect to the
 195 observations with the same angle as the one used to shift the CEOF patterns (Fig. 1e). The
 196 MJO cycle for each model is then obtained as a composite map using all the dates that lie
 197 in the given sector. As with the observations, we use the 1 standard deviation threshold for
 198 the composite map and a two-tailed t-test to estimate its statistical significance. The average

time for an MJO event to cover a complete phase of its cycle in the simulations is estimated in the same way as in the observations.

2.2.3 Wavenumber-frequency analysis and filtering

To investigate the roles of convectively coupled equatorial waves in the impact of the MJO on anomalous convection over West Africa, a wavenumber frequency spectral analysis has been performed on OLR (Wheeler and Kiladis 1999). This method is mainly used to diagnose the MJO (Wang and Schlesinger 1999 ; Wheeler and Kiladis 1999). Such method consists of separating the original OLR field into its symmetric and antisymmetric components with respect to the equator. The mean and linear trends of the deseasonalized OLR are removed in time and the ends of the series are tapered to zero. Fast Fourier Transforms (FFT) is performed first in longitude and then in time to obtain the wavenumber-frequency spectrum for each latitude. The OLR power is finally averaged over time segments and further summed over the 15°S-15°N latitude area. Hence, the strength of the different atmospheric waves in a signal can be highlighted in a wavenumber-frequency diagram for eastward and westward propagating waves (Hayashi 1982). In this work we focus on the symmetric OLR wavenumber-frequency spectra to look for convectively coupled equatorial waves.

Once the main waves are detected, the propagation of each of these waves is further analysed. We filter a given field taking only the wavenumber-frequency spectral content in certain domains corresponding to particular waves. Then, the composite analysis is repeated with this filtered field in the same way as explained above. Such approach allows us to show the propagation associated to each convectively coupled equatorial waves separately.

3. Results and Discussions

3.1 Evolution of summer MJO through AMIP simulations

3.1.1 CEOF analysis

The observed and simulated spatial structure of the two leading CEOF modes of OLR and zonal winds at 850hPa and 200hPa as a function of longitude is shown in Figure 2. Note that for better comparison, the simulated patterns have been shifted in longitude by the angles given in Fig.1f. The pattern of the first two CEOFs from the observations represents the main

227 modes of variability over the tropics. These modes explain 22.1% and 15.5% of the total ob-
228 served variance of the filtered field during the summer period, respectively (Table 2). The
229 explained variance of the first two CEOFs is underestimated by all the models (Table 2). The
230 models NorESM1-M, BCC-CSM1-1 and CNRM-CM5 show better performance with values
231 ranging from 14.8 to 17.9% for CEOF1 and 13.8 to 14.7% for CEOF2. The CEOF modes from
232 the IPSL-CM5A-LR and IPSL-CM5A-MR show the least explained variance with 10.3% and
233 10.6% for CEOF1 and 7.4% and 7.8% for CEOF2.

234 The observed CEOF1 of OLR shows a pattern characterized by an enhanced convection over
235 the maritime continent and a decreased one over central Africa and the East Pacific Ocean,
236 while the second one exhibits a minimum of convection over the Indian Ocean. Regarding
237 the simulations, there is some disparities in the OLR patterns among the models compared
238 with the observations. For CEOF1, models are capable of simulating the observed maximum
239 convection over the Maritime Continent, though with a weaker magnitude. However, the si-
240 mulation of the maximum of observed OLR (minimum convection) located over the Eastern
241 Pacific shows much larger spread in terms of magnitude and location : the MPI-ESM-LR,
242 IPSL-CM5A-LR, MPI-ESM-MR models shift this OLR maxima towards the west, whereas
243 the NorEM1-M model simulates it more eastward with stronger anomalies. For the OLR
244 maximum over Africa, models show a more consistent behaviour among themselves and with
245 the observations. Regarding CEOF2, simulations tend to bring out enhanced convection over
246 the Pacific Ocean and decreased convection over the Indian Ocean, in agreement with the ob-
247 servations. However, this last maximum of OLR is completely missed by the IPSL-CM5A-LR,
248 IPSL-CM5A-MR and CNRM-CM models.

249 The zonal wind anomalies associated with the first two CEOFs in all models show a structure
250 close to the observed one (Figure 2). At low (high) levels the first CEOF component shows
251 a maximum (minimum) of zonal wind anomalies over the Indian Ocean while the minimum
252 (maximum) is located across the Pacific basin. CEOF2 of zonal wind shows a pattern similar
253 to CEOF1 but shifted 60° to 120° to the east. The BCC-CSM1-1 tends to overestimate wind
254 anomalies, whereas the IPSL-CM5A-MR model tends to underestimate them with regards to
255 the observations.

256 Compared to the observations, models show better performance in simulating zonal wind
257 anomalies at low and high levels associated with the first two CEOFs than OLR anomalies.

We speculate that such a poor performance and disparity among models in simulating OLR anomalies could be related to the different convection schemes used by them (Table 1). Some of the most important physical processes as convection and cloud formation are represented through parameterisations. Randall et al. (2007) and Guilyardi et al. (2009) show that large systematic errors in climate simulations come mainly from the cloud parameterization used by the models.

The two first observed CEOF modes are not independent. Their lead-lag correlation shows that CEOF1 leads CEOF2 (Figure 3). In accordance with Wheeler and Hendon (2004) such result suggests an eastward propagation of the convection and wind anomalies show in Figure 2 and can be used to capture the summer MJO. For the observations, the maximum correlation of 0.75 is obtained at a lag of 9 days. Regarding the simulations, models show a maximum of correlation ranging from 0.40 to 0.75 with a time lag of between 7 and 10 days. All models agree among themselves and with the observations in the eastward propagation of the convection and the wind anomalies shown in Figure 2, because they either show that PC1 leads PC2 (MPI-ESM-LR, MPI-ESM-MR, MRI-CGCM3, BCC-CSM1-1, BCC-CSM1-1-M and CMCC-CM), or that minus PC2 leads PC1 (IPSL-CM5A-LR, IPSL-CM5A-MR, CNRM-CM5 and HadGEM2-A models). Such results also suggest that in the models the first two CEOFs are capturing the summer MJO and can be use to build the MJO cycle.

3.1.2 MJO composite cycle

To further analyse the simulation of intraseasonal variability associated with the MJO, in Figure 4 we show the composites of the deseasonalized OLR anomalies throughout the eight phases of the MJO cycle for the observations and the ensemble average of models. For the observations, at phase 1 there are negative OLR anomalies centered over the Indian Ocean and positive ones over the western Pacific. The negative anomalies strengthen at phase 2 and move northward over the Indian Continent and eastward along the equator from phase 3 to 5. At phase 6 the anomalous negative OLR dissipates over the maritime continent and extends over the Pacific basin. Positive OLR anomalies develop over the Indian Ocean at phase 5 which brings out the transition from the active to the suppressed convection moving to the central and eastern Pacific from phase 6 to 1. The ensemble average of models captures a clear eastward propagating signal in phase with the observed one, though with a weaker magnitude.

Over the Indian Ocean the models locate the events of strong and weak convection more southward with respect to the observations and, although they simulate a northward propagation into the Indian continent, it does not penetrate further than north India.

In addition each of the models taken individually captures reasonably well the observed features of the eastward propagation of the MJO signal (Figure S1 to S6). Some models like the IPSL-CM5A-LR, IPSL-CM5A-MR, HadGEM2-A, CNRM-CM5 and CMCC-CM show a weak convective signal in terms of the evolution and the amplitude and simulate an eastward propagation less coherent with regards to the observations. The northward propagation over the Indian Ocean is not clearly highlighted in most of these models and is slower compared to the observations.

The spatial correlation between the observed and modelled tropical (15°S - 15°N) OLR patterns are shown in Figure 5a. The correlations show strong and significant values above 0.4 for most of the models (ENS, BCC-CSM1-1, BCC-CSM1-1-M, CNRM-CM5, IPSL-CM5A-LR, MPI-ESM-LR, MPI-ESM-MR, MRI-CGCM3 and NorESM1-M). CMCC-CM and IPSL-CM5A-MR simulated correlations ranging between 0.2 and 0.4 while it drops below 0.2 for HadGEM2-A model. Most of those models with higher pattern correlation with respect to the observations tend also to be those that show a stronger lead-lag correlation between the Principal Components of CEOF1 and CEOF2 (Fig. 5b). The MJO signal in the simulations tends to propagate faster than in the observations (it takes them roughly 4.3 to 4.8 days to cover each phase compared to the 4.8 days per phase in the observations) except for the MRI-CGCM3 and IPSL-CM5A-MR models, which show a slower propagation (approximately 4.9 days per phase) (Table 2).

In brief 5 out of the 11 models (NorESM1-M, MRI-CGCM3, BCC-CSM1-1, BCC-CSM1-1-M and MPI-ESM-MR) used are in good agreement with the observations in representing the main features of the evolution and propagation of the MJO pattern (correlation of the composites). A wide spread has also been noticed in the rest of the models which mainly simulated a weaker MJO signal with less coherency in the eastward propagation of the signal.

3.2 Impacts of MJO over West Africa

Over West Africa, the observations show strong negative OLR anomalies (enhanced convection) during phases 1 and 2, and strong positive ones (reduced convection) during phases 4 and 5 (Fig. 4). In average, the models reproduce the timing of the enhanced convection but shift to phases 5 and 6 the main positive OLR anomalies over West Africa (Fig. 4). To analyse the performance of individual models, in Fig. 6 we show the OLR composite maps over West Africa for all models in phases 1 and 5 as representative of the strong and weak convection phases over the region, respectively. Regarding the phasing, models agree with the observations with intense negative OLR anomalies during phase 1 and strong positive ones during phase 5 (Fig. 6). The main exception is the MRI-CGCM3 model, which shows very weak positive anomalies simulated over West Africa and an inconsistent pattern in phase 5 (Fig. 6). Regarding the pattern, the multi-model mean shows OLR anomalies consistent with the observed ones in both phases. However, the individual models show more discrepancies (Fig. 6) : the main positive and negative anomalies are shown south of 10°N in the IPSL-CM5A-LR and MPI-ESM-MR models. For some models, the magnitude of the OLR anomalies over West Africa is underestimated (e.g. IPSL-CM5A-MR, CMCC-CM models).

The MJO signal also shows an impact on rainfall over West Africa. In Fig. 7, we present the spatial distribution of rainfall composites for the observations (top) and the ensemble average of the simulations (bottom) during the phases with the strongest and weakest observed MJO impact over West African convection (phases 1 and 5, respectively). The impact of the summer MJO on rainfall over West Africa is stronger during the strong convective phase of the MJO signal (above 2mm/day in some locations) than during the weak convection phase. The maximum positive and negative rainfall anomalies during phases 1 and 5 are located over the Gulf of Guinea (Fig. 7) and propagate northwards during phase 2 and 5, respectively (not shown). The ensemble average underestimates rainfall anomalies in both phases (Fig. 7), which could be related to the averaging of model outputs. It shows a higher impact of the MJO in the strong convection phase over the continental areas, where there is a high consistency among the models in the sign of the anomalies (especially over Nigerian and Cameroon highland and over the Northeast of Soudanian zone) (Fig. 7). In the weak convection phase over West Africa, models agree among themselves and with the observations showing the main rainfall anomalies over the Gulf of Guinea.

347 To evaluate the timing of the rainfall anomalies simulated over West Africa by the individual
 348 models, in Figure 8 we present the observed and simulated composites of rainfall averaged
 349 over West Sahel (20°W - 10°E and 10°N - 20°N) and Guinean zone (12°W - 6°E and 4°N - 7°N)
 350 respectively. For the observations, over West Sahel, the phases 1, 2, 3, 7 and 8 are associated
 351 with wet conditions while drier conditions occur during phases 4, 5 and 6. The transition phase
 352 of the MJO from negative to positive rainfall anomalies is well marked in the observed rainfall
 353 composites in both regions though it occurs one phase later over Guinean zone than over the
 354 West Sahel (between phases 7 to 8 and 6 and 7, respectively). The timing of the MJO impact
 355 on rainfall is well captured by the models : most of them simulate positive (negative) rainfall
 356 anomalies over both regions during phases 1 and 2 (5 and 6). While rainfall anomalies over
 357 Guinea are underestimated by all models, those over the West Sahel are overestimated by the
 358 CNRM-CM5 and NorESM1-M models.

359 The impact of the MJO on the AEJ during the strong and weak convective phases is presented
 360 in Figure 9. In phase 1 which corresponds to the strong convective phase, the AEJ is extended
 361 to the east. Such result suggests that the strong active convection is associated with the AEJ
 362 and its entrance region (Fig. 9). Positive anomalies are observed south of the AEJ and their
 363 extension are limited over the continent. The exit region of the jet which corresponds to the
 364 region where negative anomalies of zonal wind at 600hPa appear (30°W - 10°W)/ 10°N - 25°N)
 365 is seen to coincide with the increased convection off the coast of West Africa (Fig. 6). The
 366 weak convective phase (phase 5) is characterised by strong negative anomalies south of the
 367 core of the jet and are mainly located over the ocean. However, weak positive anomalies of
 368 zonal wind at 600hPa is observed over the exit region during the weak convective phase (Fig.
 369 6). During the strong convective phase, the ensemble average exhibits positive zonal wind
 370 anomalies at 600 hPa south of the AEJ core, which extend further into the Atlantic compa-
 371 red to the observations. Conversely, in the weak convection phase (phase 5) similar though
 372 opposite anomalies are simulated. Such westerly (easterly) anomalies south of the AEJ rela-
 373 ted to enhanced (weakened) convection over West Africa are consistent with the results from
 374 Omotosho and Abiodun (2007), who found that wet (dry) periods are associated with strong
 375 west to southwesterly (east to northeasterly) wind anomalies south of the AEJ, which could
 376 transport moisture away from the jet.

3.3 Mechanisms through which MJO impacts West Africa

Results so far presented have shown good evidence for the impact of the MJO on West African rainfall variability. Therefore, further investigations are carried out to analyse the physical mechanisms through which such impact takes place. Previous studies highlighted the roles of equatorial Kelvin and Rossby waves in MJO propagation (e.g. Matthew 2004 and Mohino et al. 2012). Roundy and Frank (2004b) have highlighted the importance of westward-propagating equatorial Rossby modes interacting with the MJO in accounting for much of the intraseasonal convective variability within the tropics.

To investigate the role of these waves a composite hovmoller diagram of 850 hPa anomalies of zonal wind (shaded), OLR (contours in Fig. 10a and Fig. 10c) and SLP (contours in Fig. 10b and Fig. 10d) averaged over the latitude between 10°S and 10°N is presented for the observations (Fig. 10a and Fig. 10b) and for the ensemble average (Fig. 10c and 10d). The observations show a clear eastward propagation of the OLR anomalies from the Indian Ocean to the western Pacific. The negative OLR anomalies (enhanced convection) are preceded by easterly winds at 850hPa and followed by westerly ones. The opposite is found for positive OLR anomalies (reduced convection). The easterly propagating OLR anomalies weaken around 160°E. From that point, the propagation of zonal wind anomalies at 850hPa is increased in speed to approximately 30 m/s, which is more consistent with a dry Kelvin wave (Milliff and Madden 1996 ; Wheeler and Kiladis 1999). In addition, beyond 120°E-150°E the negative zonal wind anomalies at 850 hPa are in phase with the negative sea level pressure ones, and vice versa, which is also suggestive of a dry Kelvin wave according to Sobel and Kim (2012). Thus, our results suggest that the enhanced (reduced) convection anomalies in the western Pacific would trigger a dry Kelvin wave that would propagate from these longitudes leading the perturbation eastward, consistently with previous works (Roundy 2012 ; Sobel and Kim 2012). Such dry Kelvin waves reach the South American coast where they seem to promote convection anomalies of the opposite sign to those that triggered the dry Kelvin waves in the Pacific Warm Pool. The speed of the propagation is reduced, the anomalies of zonal wind at 850 hPa and SLP weaken and the phasing between both variables changes, suggesting that the dry Kelvin wave does not progress further east than 60°W.

Compared to the observations, the eastward propagation of the OLR anomalies (contours) is well simulated by the ensemble average of the models over the Indian Ocean and the West

Pacific, though they show weaker anomalies (Fig. 10c). The ensemble average also shows a phasing between anomalies of zonal wind at 850hPa and sea level pressure (contours) from 120°E-150°E to the east, suggesting also the emission of a dry Kelvin wave in the models (fig. 10d), which would weaken once it arrives over South America. Sea level pressure anomalies are, nevertheless, much weaker in the simulation than in the observations, especially over Africa. In order to split out the contribution of the different equatorial coupled waves on the overall impact a wavenumber frequency spectral analysis is performed. In Figure 11 we highlight the spectral peaks by plotting the ratio of the power spectra above the background OLR spectrum (estimated as the OLR power spectrum smoothed several times in wavenumber and in frequency, see Wheeler and Kiladis 1999 for more details). The observations (Fig. 11a) show strong spectral content in the MJO band, at a frequency of around 0.025 cpd (period of approximately 40 days) for the range of eastward planetary wavenumber of 1 through to about 7. The eastward moving Kelvin waves occupy a broad region of the wavenumber-frequency regions in the 0.05 to 0.25 cpd band (periods of 4 to 20 days) (Wheeler and Kiladis 1999; Wheeler et al. 2000; Roundy and Frank 2004a) while westward Rossby waves exhibit a strong component of westward wavenumbers of 0-5 and a frequency similar to the one of the MJO. Additional analysis shows that the ensemble average of models (Fig. 11b) simulates a strong signal in the MJO band at frequency around 0.025 cpd for the range of eastward planetary wavenumber of 1 through to about 7. Nevertheless, it shows that the model's ensemble average simulates a very weak peak in the Kelvin wavenumber frequency zone compared to the observations. The spectral peak simulated by the ensemble mean in the region of Rossby waves is stronger than the observed one. The same analysis is performed also for each individual model and they mostly show a pattern similar to the observed one for MJO and Rossby components. However, only the BCC-CSM1-1 and BCC-CSM1-1-M models show a clear spectral component in the region corresponding to the convectively coupled Kelvin waves (Figure S7-S12). To further analyse the skill of each model in representing the symmetric component of the different equatorially trapped waves we present in Figure 12a the ratio of the power spectra to the background power spectrum intensity averaged over the two different boxes (red and black boxes presented in Figure 11) that represent the eastward and westward propagating convectively coupled waves. The ensemble mean is calculated by averaging over the different

models taken individually. The observations show the maximum OLR power contribution in the eastward propagating (MJO) box, followed by the westward propagating (Rossby) component. Models tend to underestimate the power spectrum corresponding to the eastward component peaks and overestimate the one in the westward box. In our sample of 11 models, only three (NorESM1-M, BCC-CSM1-1 and BCC-CSM1-1-M) show an average of OLR power in the eastward box above 1.4 times the background spectrum (the approximate content shown by the observations). In addition, and conversely to the observed behaviour (the same westward and eastward boxes), the models show an average spectrum in the westward box above the one in the eastward box, except for the BCC-CSM1-1 model.

In order to separate the role played by the different propagating waves in the convection signal obtained over West Africa we repeat the composite procedure with OLR fields that are previously filtered for the westward and eastward regions (defined in Fig. 11) of the wavenumber-frequency spectral content. We leave out the convectively Kelvin wave component from this analysis because our definition of the MJO signal, which is based on fields filtered in the 20 to 90 day band (0.011 to 0.05 cpd), is effectively filtering out those waves with a frequency higher than 0.05 cpd (periods lower than 20 days). This methodology can then only separate the westward propagating component, which we have identified as the convectively coupled Rossby wave, and the eastward propagating component, which we have identified with the MJO. We can not rule out that some convectively coupled Kelvin waves with very low frequencies (lower than 0.05 cpd) and equivalent depths from 8 to 90 m could be included in the eastward propagating signature.

In addition, we represent in figure 12b the correlation between the composite of unfiltered and filtered OLR fields taking into account the entire tropics between 15°S-15°N and all eight phases of MJO. In the observations, the main contribution to the MJO tropical signal shown in Fig.4a comes from the eastward propagating signal or MJO (correlation between the original composite and the one obtained when filtering in the MJO area of the wavenumber-frequency spectral content is 0.78). However, there is also a contribution from the westward propagating signal we have termed convectively coupled Rossby waves (correlation of 0.40) and both together explain a higher percentage of the tropical convection signal (correlation of 0.85). In the models, the spacial correlation between the overall signal and the one coming from the eastward propagating part tend to be lower than for the observations, ranging from 0.47 to 0.78 (Fig.

12b). Such correlation tends to be higher for those models with a stronger spectral peak in the MJO region (Fig. 12d). In addition, the higher the dominance of the eastward propagating signal in the modelled composite, the likelier a better resemblance of the simulated tropical signal with the observed composite (Fig. 12c). The correlation between the overall signal and the part coming from the westward propagating signal tends to be higher in the models than in the observations, with 7 models out of 11 (IPSL-CM5A-LR, IPSL-CM5A-MR, MPI-ESM-MR, HadGEM2-A, CNRM-CM5, IPSL-CM5A-MR and MPI-ESM-LR) showing a correlation higher than 0.40. In most models the overall MJO signal is dominated by the eastward propagating component, as in the observations (Fig. 12a). When the OLR fields are filtered using both the eastward and westward propagating components of the spectra, the correlations are higher than when using only one of both components (Fig. 12a). These results suggest that the westward equatorial Rossby waves are relevant to explain the overall impact of the MJO over West Africa, in accordance with previous studies (Roundy et al. 2004b; Mohino et al. 2012).

4. Conclusions

This research study was conducted using a set of simulations from AMIP experiments to investigate the relationship between MJO and the West African monsoon during the boreal summer and also to assess the performance of the models in simulating such link. The study evaluated the impact of the MJO on convection and rainfall in the region and investigated the dynamical processes involved.

Our results show that the AMIP-type simulations from the 11 models we have analysed are able to simulate an eastward propagating signal in the tropics linking a barotropic wavenumber 1 structure in zonal winds with anomalies in convection. Such structure can account for a relevant part of the models intraseasonal variability (between 17.7 % to 32.6 %, depending on the model) in the 20-90 day band, which is in all cases smaller than for the observations (37.6%). We have identified such structure with the MJO and we have further research into its signature in convection in the tropics with a special focus on West Africa. The speed of propagation of such MJO in the models (from 36 to 39 days to complete a whole cycle) is close to the observed one (38.4 days to complete a cycle).

Regarding its impacts over West Africa, we have shown that, in accordance with the observations, the models tend to show two distinct phases with strong and weak convection, respectively, which are, in turn, connected to positive and negative rainfall anomalies, especially over the Gulf of Guinea, suggesting that the MJO can impact West African rainfall intraseasonal variability during the summer period. In general, the pattern of impact of the MJO signal on convection over West Africa is simulated by most of the models. However, the big challenge is the large variability of rainfall over West Africa. The MJO-West Africa relationship is further confirmed by the link between the MJO disturbances and the AEJ anomalies, particularly over the coastal regions.

The present study also found that the observed time lag between the positive/negative convection anomalies over the Indian Ocean and West Africa is about 15-20 days. That time lag correlation is well simulated by some models (NorESM1-M, MPI-ESM-MR, BCC-CSM1-1, IPSL-ESM-LR and CNRM-CM5) while others show longer values ranging from 20 to 25 days. Regarding the mechanisms, our study suggests that the main impact of the MJO over West Africa is due to the eastward propagating part of the signal. Most of the tropical convection pattern can be obtained with just this component. However, we have also shown that the westward equatorial Rossby waves play a relevant role both in models and in the observations in the overall impact on convection over West Africa, in agreement with the work of Mohino et al. (2012). The simulations also show that the contrast between the Indian Ocean and West Africa in terms of the anomalous convection might be used as a potential predictor since the results show a time lag of about 15-20 and/or 20-25 days between the two regions. The AMIP simulations suggest then a potential to predict occurrences of wet and dry sequences over West Africa if the MJO can be realistically predicted (Waliser et al. 1999; Jones et al., 2004b).

Acknowledgements

This work was supported by the Agencia Estatal Consejo Superior de Investigaciones Cientificas (CSIC) of Spain via program : I-COOP+ reference COOPA20029 and the German Federal Ministry of Education and Research (BMBF) via WASCAL (West African Science Service Center on Climate Change and Adapted Land Use) project coordinated by the Center for Development Research (ZEF, Bonn University), and implemented in a collaborative effort

530 by West African and German partners. Additional support was provided by the Universi-
531 dad Complutense de Madrid (UCM) via the collaboration between TROPA-UCM-IGEO and
532 LPAO-SF (Laboratoire de Physique de l'Atmosphere et de l'Ocean Simeon Fongang) group :
533 project 63 from the IX UCM Call for Cooperation and Development Projects 2012. The au-
534 thors thank a lot the group TROPA (Tropical Atlantic Variability Group) from UCM for all
535 the support they provide us to fulfill this work. The research leading to these results has
536 received funding from the European Union Seventh Framework Programme (FP7/2007-2013)
537 under grant agreement n° 603521 and the Spanish project CGL2012-38923-C02-01. We ack-
538 nowledge the World Climate Research Programme's Working Group on Coupled Modelling,
539 which is responsible for CMIP, and we thank the climate modelling groups for producing
540 and making available their model outputs. For CMIP the U.S. Department of Energy's Pro-
541 gram for Climate Model Diagnosis and Intercomparison provides coordinating support and
542 led development of software infrastructure in partnership with the Global Organization for
543 Earth System Science Portals. Thanks also to NOAA for providing the Outgoing Longwave
544 Radiation (OLR) data.

546 References

- 547 — Barlow M, Wheeler M, Lyon B and Cullen H (2005) Modulation of daily precipitation
548 over southwest Asia by the Madden-Julian oscillation. *Mon. Wea. Rev.* 133 :3579-3594
- 549 — Bond NA and Vecchi GA (2003) The influence of the Madden-Julian Oscillation (MJO)
550 on Precipitation in Oregon and Washington, *Wea. Forecasting* 18(4) : 600-613
- 551 — Carvalho L, Jones C and Liebmann B (2004) The South Atlantic convergence zone :
552 Intensity, Form, Persistence, and relationships with intraseasonal to interannual activity
553 and extreme rainfall. *J. Clim* 17 :88-108
- 554 — CLIVAR Madden-Julian Oscillation Working Group (2009) MJO simulation diagnos-
555 tics. *J. Clim* 22 : 3006-303. DOI : 10.1175/2008JCLI2731.1
- 556 — Crueger T, Stevens B and Brokopf R (2013) The Madden-Julian oscillation in ECHAM6
557 and the introduction of an objective MJO metric, *J. Clim* 26 : 3241-3257. DOI :
558 10.1175/JCLI-D-12-00413.1
- 559 — Dee DP and Uppala S (2009) Variational bias correction of satellite radiance data in
560 the ERA-interim reanalysis. *Q.J.R Meteorol Soc.* 135 :1830-1841
- 561 — Donald A and Coauthors (2006) Near-global impact of the Madden-Julian Oscillation
562 on rainfall. *Geophysical Research Letters* 33 : L09704, doi : 10.1029/2005GL025155
- 563 — Gadgil S and Rao PRS (2000) Farming strategies for a variable climate-a challenge.
564 *Curr Sci.* 78 :1203-1215
- 565 — Guilyardi E, Wittenberg A, Fedorov A, Collins M, Wang C, Capotondi A, van Olden-
566 borgh GJ and Stockdale T (2009) Understanding El Nino in ocean-atmosphere general
567 circulation models : Progress and challenges, *Bull. Am. Meteorol. Soc* 90 :325-340
- 568 — Hayashi Y (1982) Space-time spectral analysis and its applications to atmospheric
569 waves. *J. Oceanogr. Soc. Jpn.* 60 :156-171
- 570 — Hendon H H, Zhang CD and Glick JD (1999) Interannual variation of the Madden-
571 Julian oscillation during austral summer. *J. Clim* 12 :2538-2550
- 572 — Higgins W, Schemm J, Shi W and Leetmaa A (2000) Extreme precipitation events in
573 the western United States related to tropical forcing. *J. Clim* 13 :793-820
- 574 — Huffman GJ, Adler RF, Morrissey MM, Bolvin DT, Curtis S, Joyce R, McGavock B,

- Susskind J (2001) Global precipitation at one-degree daily resolution from multisatellite observations. *J Hydrometeor* 2 :36-50
- Hung MP, Lin JL, Wang W, Kim D, Shinoda T and Weaver SJ (2013) MJO and Convectively Coupled Equatorial Waves Simulated by CMIP5 Climate Models. *J. Clim* 26 :6185-6214. doi : <http://dx.doi.org/10.1175/JCLI-D-12-00541.1>
- Janicot S and Sultan J (2001) Intra-seasonal modulation of convection in the West African monsoon. *Geophys Res Lett.* 28 : 523-526
- Janicot S, Mounier F, Gervois S, Hall JN, Leroux S, Sultan B and Kiladis GN (2009) The Dynamics of the West African Monsoon. Part IV : Analysis 25-90-day variability of convection and the role of the Indian monsoon. *J. Clim* 22 :1541-1565. DOI : 10.1175/2008JCLI2314.1
- Jones C and Schemm JE (2000) The influence of intraseasonal variations on medium-to extended-range weather forecasts over South America. *Mon. Weather. Rev.* 128 :486-494
- Jones C, Waliser DE, Lau WK and Stern W (2000) Prediction skill of the Madden and Julian Oscillation in dynamical extended range forecasts. *Clim. Dyn* 16 :273-289
- Jones C, Waliser DE, Lau WK and Stern W (2004a) The Madden-Julian oscillation and its impact on Northern Hemisphere weather predictability. *Mon. Weather. Rev.* 132 :1462-1471
- Jones C, Carvalho LMV, Higgins RW et al (2004b) Statistical forecast skill of tropical intraseasonal convective anomalies. *J. Clim* 17 :2078-2095
- Kessler WS (2001) EOF representations of the Madden-Julian Oscillation and its connection with ENSO. *J. Clim* 14 :3055-3061
- Kim D, Sperber K, Stern W, Waliser D, Kang IS, Maloney E, Schubert S, Wang W, Weickmann K, Benedict J, Khairoutdinov M, Lee MI, Neale R, Suarez M, ThayerCalder K and Zhang G (2009) Application of MJO simulation diagnostics to climate models. *J. Clim* 22 :6413-6436
- Knutson T and Weickmann K (1987) 30-60 day atmospheric oscillations : Composite life cycles of convection and circulation anomalies. *Mon. Wea. Rev* 115 :1407-1436
- Lavender SL and Matthews AJ (2009) Response of the West African monsoon to the Madden-Julian oscillation. *J. Clim* 22 :4097-4116

- Liebmann B, Hendon HH and Glick JD (1994) The relationship between tropical cyclones of the western Pacific and Indian Oceans and the Madden-Julian oscillation. *J. Meteor. Soc. Japan* 72 :401-411
- Liebmann B and Smith CA (1996) Description of a complete (interpolated) outgoing longwave radiation dataset. *Bull. Amer. Meteor. Soc* 77 :1275-1277
- Liebmann B, Kiladis GN, Vera CS, Saulo AC and Carvalho LMV (2004a) Subseasonal variations of rainfall in South America in the vicinity of the low-level jet east of the Andes and comparison to those in the South Atlantic convergence zone. *J. Clim* 17 :3829-3842
- Lin JL, Kiladis GN, Mapes BE, Weickmann KM, Sperber KR, Lin W, Wheeler MC, Schubert, SD, Del Genio A, Donner LJ, Emori S, Gueremy JF, Hourdin F, Rasch PJ, Roeckner E and Scinocca JF (2006) Tropical intraseasonal variability in 14 IPCC AR4 climate models. Part I : Convective signals. *J. Clim* 19 :2665-2690, doi :10.1175/JCLI3735.1
- Madden RA and Julian PR (1971) Description of a 40-50 day oscillation in the zonal wind in the tropical Pacific. *J. Atmos. Sci* 28 :702-708
- Madden RA and Julian PR (1994) Detection of a 40-50 day oscillation in the zonal wind in the tropical Pacific. *Mon. Weather. Rev* 122 :813-837
- Maloney E and Hartmann D (2000) Modulation of eastern North Pacific hurricanes by the Madden-Julian Oscillation, *J. Clim* 13 :1451-1460
- Maloney E and Shaman J (2008) Intraseasonal Variability of the West African Monsoon and Atlantic ITCZ. *J. Clim* 12 :2898-2918
- Mauritsen T and Coauthors (2012) Tuning the climate of a global model. *J. Adv. Model. Earth Syst* 4 : M00A01, doi : 10.1029/2012MS000154
- Matthews A (2004) Intraseasonal variability over the tropical Africa during northern summer. *J. Clim* 17 :2427-2440
- Mohino E, Janicot S, Douville H and Li ZXL (2012) Impact of the Indian part of the summer MJO on West Africa using nudged climate simulations. *Clim. Dyn* 38 : pp. 2319-2334 DOI :10.1007/s00382-011-1206-y
- Mounier F and Janicot S (2004) Evidence of two independent modes of convection at intraseasonal timescale in the West African summer monsoon. *Geophys. Res. Lett* 31 : L16116, doi : 10.1029/2004GL020665

- Mounier F, Kiladis GN and Janicot S (2007) Analysis of the dominant mode of convectively coupled Kelvin waves in the West African monsoon. *J. Clim* 20 :1487-1503
- Milliff RF and Madden RA (1996) The existence and vertical structure of fast, eastward-moving disturbances in the equatorial troposphere. *J. Atmos. Sci* 53 :586-597
- Omotosho JB and Abiodun BJ (2007) A numerical study of moisture build-up and rainfall over West Africa. *Meteorological Applications* 14(3) : 209-225
- Pohl B, Janicot S, Fontaine B and Marteau R (2009) Implication of the Madden-Julian oscillation in the 40-day variability of the West African monsoon. *J. Clim* 22 :3769-3785
- Randall DA et al. (2007) Climate models and their evaluation. *Climate Change 2007 : The Physical Science Basis. Contribution of Working Group I to the Fourth Assessment Report of the Intergovernmental Panel on Climate Change*, S. Solomon et al., Eds., Cambridge University Press, Cambridge, U. K., 589-662.
- Roundy PE. and Frank WM (2004a) A climatology of waves in the equatorial region. *J. Atmos. Sci* 61 :2105-2132
- Roundy PE. and Frank WM (2004b) Effects of low-frequency wave interactions on intraseasonal oscillations. *J. Atmos. Sci* 61 :3025-3040
- Roundy PE (2012) Observed Structure of Convectively Coupled Waves as a Function of Equivalent Depth : Kelvin Waves and the Madden-Julian Oscillation. *J. Atmos Sci* 69 :2097-2106, DOI : 10.1175/JAS-D-12-03.1
- Slingo JM and Coauthors (1996) Intraseasonal oscillation in 15 atmospheric general circulation models : Results from an AMIP diagnostic subproject. *Clim. Dyn* 12 : 325-357
- Sobel AH and Kim D (2012) The MJO-Kelvin wave transition, *Geophys. Res. Lett.* 39 : L20808, doi :10.1029/ 2012GL053380
- Sultan B, Janicot S and Diedhiou A (2003) The West African monsoon dynamics. Part I : documentation of intraseasonal variability. *J. Clim* 16 : 3390-3406
- Sultan B, Baron C, Dingkuhn M, Sarr B, Janicot S (2005) Agricultural impacts of large-scale variability of the West African monsoon. *Agric. For. Meteorol.* 128 : 93-110
- Taylor KE, Stouffer RJ and Meehl GA (2012) An overview of CMIP5 and the experiment design, *Bull. Am. Meteorol. Soc.* 93 :485-498, doi :10.1175/BAMS-D-11-00094.1
- Uppala SM et al. (2005) The ERA-40 re-analysis. *Q.J.R Meteorol Soc.* 131 : 2961-3012

- Venegas SA (2001) Statistical methods for signal detection in climate. Danish Center for Earth System Science.
- Ventrice MJ, Thorncroft CD and Roundy PE (2011) The Madden Julian's Oscillation on African easterly waves and downstream tropical cyclogenesis. *Mon. Wea. Rev.* 139 :2704-2722
- Waliser DE, Lau KM and Kim JH (1999b) The influence of coupled sea surface temperatures on the Madden-Julian Oscillation : A model perturbation experiment. *J. Atmos. Sci.* 56 : 333-358
- Waliser DE and Coauthors (2003) AGCM simulations of intraseasonal variability associated with the Asian summer monsoon. *Clim. Dyn.* 21 : 423-446
- Wang W and Schlesinger ME (1999) The dependence on convective parameterization of the tropical intraseasonal oscillation simulated by the UIUC 11-layer atmospheric GCM. *J. Clim* 12 :1423-1457
- Wheeler M and Kiladis GN (1999) Convectively coupled equatorial waves : analysis of clouds and temperature in the wavenumber- frequency domain. *J. Atmos. Sci.* 56 : 374-399
- Wheeler M, Kiladis GN and Webster PJ (2000) Large-scale dynamical fields associated with convectively coupled equatorial waves. *J. Atmos. Sci.* 57 : 613-640
- Wheeler M and Hendon H (2004) An all-season real-time multivariate MJO index : development of an index for monitoring and prediction. *Mon. Weather Rev.* 132 : 1917-1932
- Wheeler MC and McBride JL (2005) Australian-Indonesian monsoon, in *Intraseasonal Variability of the Atmosphere-Ocean Climate System*. W. K. M. Lau and D. E. Waliser, Eds., Praxis Publishing, Chichester, pp 436
- Yasunari T (1979) Cloudiness fluctuations associated with the northern hemisphere summer monsoon. *J. Meteor. Soc. Jpn.* 57 : 227-242
- Zhang CD (2005) Madden-Julian oscillation. *Rev. Geophys.* 43 :RG2003. doi 10.1029 / 2004RG000158.
- Zhang C, Dong M, Gualdi S, Hendon HH, Maloney ED, Marshall A, Sperber KR And Wang W (2006) Simulations of the Madden-Julian Oscillation in four pairs of coupled and uncoupled global models, *Clim. Dyn.* 27 :573-592, doi :10.1007/s00382-006-0148-2

699 List of Tables

700	1	Summary of models, their assigned numbers, number of integrations (number	
701		of years for each simulation multiplied by the number of ensemble members	
702		used), horizontal resolutions, convections schemes and the different institutes	
703		involved for the analysis.	26
704	2	Explained variance of the first two CEOFs of filtered data and the inverse of	
705		phase speed of the MJO cycle from the observations and simulations.	27

TABLE 1 – Summary of models, their assigned numbers, number of integrations (number of years for each simulation multiplied by the number of ensemble members used), horizontal resolutions, convections schemes and the different institutes involved for the analysis.

Models	Assigned numbers	Numb of integration	LatxLon	Convect schemes	Institute
BCC-CSM1-1	1	30	2.8°x2.8°	Tongwen Wu (2012)	Beijing Climate Center, China Meteorological Administration
BCC-CSM1-1-M	2	30	1.1°x1.25°	Tongwen Wu (2012)	Beijing Climate Center, China Meteorological Administration
CMCC-CM	3	30*3	0.75°x0.75°	Tiedtke (1989)/Nordeng (1994)	Centro Euro-Mediterraneo per I Cambiamenti Climatici
CNRM-CM5	4	30	1.4°x1.4°	Philippe Bougeault (1985)	Centre National de Recherches Meteorologiques
HadGEM2-A	5	30	1.25°x1.875°	Maidens and Derbyshire (2006)	Met Office Hadley Centre
IPSL-CM5A-LR	6	30*6	1.875°x3.75°	Emanuel (1991)	Institut Pierre-Simon Laplace
IPSL-CM5A-MR	7	30*4	1.25°x2.5°	Emanuel (1991-1993)	Institut Pierre-Simon Laplace
MPI-ESM-LR	8	30*4	1.8°x1.875°	Roeckner <i>et al.</i> (2003)	Max Planck Institute for Meteorology (MPI-M)
MPI-ESM-MR	9	30*4	1.8°x1.875°	Tiedtke (1989)/ Nordeng (1994)	Max Planck Institute for Meteorology (MPI-M)
MRI-CGCM3	10	30	1.1°x1.1°	Yukimoto <i>et al.</i> (2011)	Meteorological Research Institute
NorESM1-M	11	30*3	1.9°x2.5°	Bentsen <i>et al.</i> (2012)	Norwegian Climate Centre

TABLE 2 – Explained variance of the first two CEOFs of filtered data and the inverse of phase speed of the MJO cycle from the observations and simulations.

Models	CEOF1 (%)	CEOF2 (%)	Inverse of Phase Speed (days per phase)
NOAA/ERA-40/ERA-Interim	22.1	15.5	4.8
BCC-CSM1-1	17.9	14.7	4.7
BCC-CSM1-1-M	15.0	12.6	4.3
CMCC-CM	12.6	10.5	4.5
CNRM-CM5	14.8	14.2	4.8
HadGEM2-A	11.5	9.0	4.7
IPSL-CM5A-LR	10.3	7.4	4.6
IPSL-CM5A-MR	10.6	7.8	4.9
MPI-ESM-LR	12.7	10.3	4.8
MPI-ESM-MR	13.2	10.9	4.6
MRI-CGCM3	15.7	12.2	4.9
NorESM1-M	17.3	13.8	4.3

706 List of Figures

707	1	Zonal wind anomalies at 850hPa (m/s per standard deviation of the PC) cor-	
708		responding to the first (a) and second (b) CEOF modes for the observations	
709		(solid black line) and CNRM-CM5 simulation (solid red line). The red dashed	
710		line shows the modelled pattern shifted by 72° in longitude. c) Lead-lag corre-	
711		lation in longitude between the six CEOF patterns (three variables times two	
712		CEOF modes) for the observations and CNRM-CM5 model. The maximum	
713		correlation obtained at 72° east is highlighted in grey. d) The eight sectors in	
714		which the PC1-PC2 observed phase space is divided in order to build the com-	
715		posite maps. The circle shows the one standard deviation threshold used for	
716		the composite analysis. e) The eight sectors in which the PC1-PC2 phase space	
717		from the CNRM-CM5 model is divided in order to build the composite maps.	
718		The circle shows the one standard deviation threshold used for the composite	
719		analysis. f) Angles used to shift the CEOF patterns and the phase space for	
720		each model (see details in the text).	31
721	2	Observed (thick black line) and simulated first two CEOFs of summer OLR	
722		and zonal wind at 850hPa and 200hPa anomalies from AMIP simulations. The	
723		first line of figures represent OLR, the second one the zonal wind at 200hPa	
724		and the last one the zonal wind at 850hPa anomalies. The units are W/m^2 per	
725		standard deviation of the associated first two CEOFs for OLR and m/s per	
726		standard deviation for zonal wind.	32
727	3	Lead-lag correlations between the principal components associated with the first	
728		and second CEOF from observation and AMIP simulations. The x-axis of this	
729		figure is in days while the y-axis represents the lead-lag correlation coefficients	
730		between PC1 and PC2.	33
731	4	Summer composites of deseasonalized anomalies of OLR according to the eight	
732		phases associated with the MJO, from observations (left) and the ensemble	
733		average of AMIP simulations (right). The units are W/m^2 . The grey contours	
734		represent the 95% significant regions obtained from a two-tailed t-test.	34

735	5	a- Correlations of summer composites of deseasonalized OLR anomalies between the observations and AMIP simulations in the tropics (15°S-15°N). b-	
736		Scatterplot between the maximum lead lag correlation of the first two principal	
737		Components (PC1 and PC2) and the correlation coefficients between the ob-	
738		servations and each of AMIP's models in the tropics presented in plot a). The	
739		red line in b) delimits the observed maximum lead lag correlation value. For	
740		convenience numbers are associated to the different models used through this	
741		study (see table 1).	35
742	6	Summer composites of observed deseasonalized anomalies of OLR (W/m^2) over	
743		West Africa during the strong (1) and weak (5) convective phases of MJO from	
744		the observations, individual AMIP simulations and the ensemble average of	
745		models. Red lines represent the 95% significant regions obtained from a two-	
746		tailed t-test.	36
747	7	Composites of rainfall anomalies (mm/day) during the MJO strong (a and c)	
748		and weak (b and d) convective phases over West Africa for the observations (a	
749		and b) and the ensemble average (c and d) of the models. The crosses mark the	
750		areas where at least eight (8) out of 11 models are consistent on the sign of the	
751		composite. Grey contours represent the area where rainfall anomalies are 95%	
752		significant according to a two-tailed t-test.	37
753	8	Composites of observed and simulated deseasonalized rainfall (mm/day) ano-	
754		malies averaged over the Sahel (20°W-10°E and 10°N-20°N) and Guinean Coast	
755		(12°W-6°E and 4°N-7°N) boxes for each phase in the observations, models and	
756		the ensemble average. The composites are averaged over the different boxes	
757		according to the different eight phases of MJO.	38
758	9	Composites of zonal wind anomalies (m/s) at 600hPa (shaded) during the strong	
759		(a and c) and weak (b and d) convective phases of MJO from the observations	
760		(a and b) and the ensemble average of models (c and d) over West Africa.	
761		The green contour lines represent the climatological zonal wind at 600hPa. The	
762		crosses mark the areas where at least eight (8) out of 11 models are consistent	
763		on the sign of the composite. Grey contours represent the area where the zonal	
764		wind anomalies at 600hPa are 95% significant according to a two-tailed t-test. .	39
765			

766	10	Hovmoller diagram performed over the composite of deseasonalized anomalies	
767		averaged between 10°S and 10°N of zonal wind at 850hPa (m/s), OLR (W/m^2)	
768		and SLP (hPa) for observation (Fig. 10a and Fig. 10b) and simulations (Fig. 10c	
769		and Fig. 10d). Wind anomalies are shaded. The black solid contours represent	
770		the negative anomalous values of OLR (SLP) while the red solid contours high-	
771		light the positive ones in Fig. 10a and Fig. 10c (Fig. 10b and Fig. 10d). The	
772		grey lines represent the contour zero for OLR (Fig. 10a and Fig. 10c) and SLP	
773		(Fig. 10b and Fig. 10d). The OLR values vary from -16 to $16W/m^2$ while SLP's	
774		contours are ranging from -1 to 1hPa. The intervals between lines is $4 W/m^2$	
775		for OLR values and 0.2hPa for SLP's values.	40
776	11	Wavenumber frequency spectral analysis of OLR data from the observations (a)	
777		and the ensemble average of models (b). The eastward part of the signal (MJO)	
778		is extracted from 0 to 9 (see black box) of the periods of roughly 30-90 days and	
779		the westward part (corresponding to the Rossby waves) is extracted from -10	
780		to 1 (see red box). The units are the ratio of the power spectra above the back-	
781		ground OLR spectrum obtained after smoothing several times in wavenumber	
782		and in frequency.	41
783	12	a) Observed and simulated spectrum intensity above the background averaged	
784		over the different equatorial waves boxes (eastward and westward component)	
785		defined in figure 11. b) Spatial correlation in the tropics between MJO compo-	
786		sites of unfiltered OLR and filtered OLR fields using the eastward and westward	
787		boxes defined in figure 11. c) Scatterplot between the correlation coefficients	
788		between the observations and each of AMIP's models in the tropics and the	
789		composites of deseasonalized OLR filtered over MJO's wavenumber-frequency	
790		box. The brown line in c delimits the observed value of the composites of desea-	
791		sonalized OLR filtered over MJO's wavenumber-frequency box. d) Scatterplot	
792		between the strength of MJO and the composites of deseasonalized OLR filtered	
793		over MJO's wavenumber-frequency box.	42

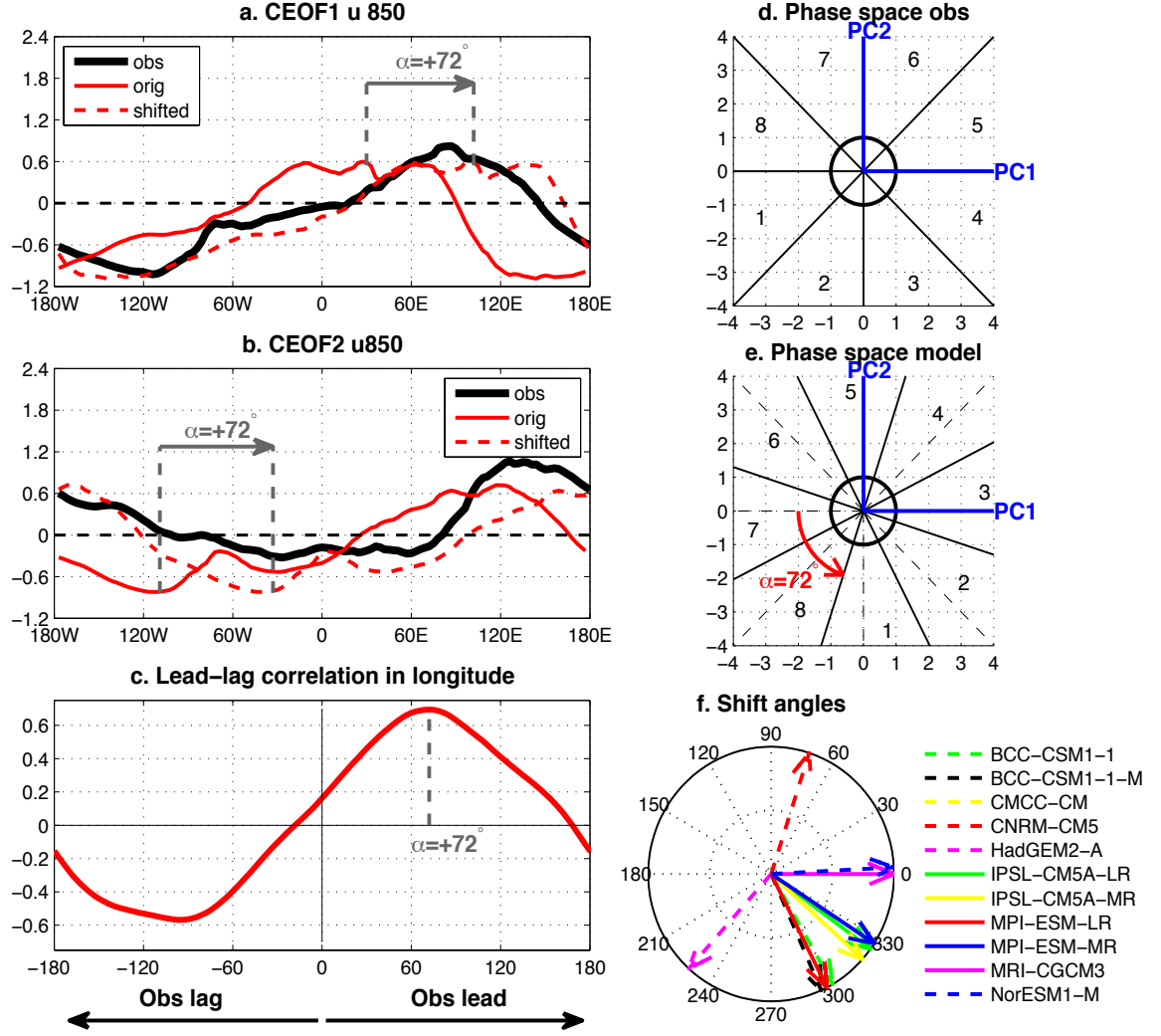


FIGURE 1 – Zonal wind anomalies at 850hPa (m/s per standard deviation of the PC) corresponding to the first (a) and second (b) CEOF modes for the observations (solid black line) and CNRM-CM5 simulation (solid red line). The red dashed line shows the modelled pattern shifted by 72° in longitude. c) Lead-lag correlation in longitude between the six CEOF patterns (three variables times two CEOF modes) for the observations and CNRM-CM5 model. The maximum correlation obtained at 72° east is highlighted in grey. d) The eight sectors in which the PC1-PC2 observed phase space is divided in order to build the composite maps. The circle shows the one standard deviation threshold used for the composite analysis. e) The eight sectors in which the PC1-PC2 phase space from the CNRM-CM5 model is divided in order to build the composite maps. The circle shows the one standard deviation threshold used for the composite analysis. f) Angles used to shift the CEOF patterns and the phase space for each model (see details in the text).

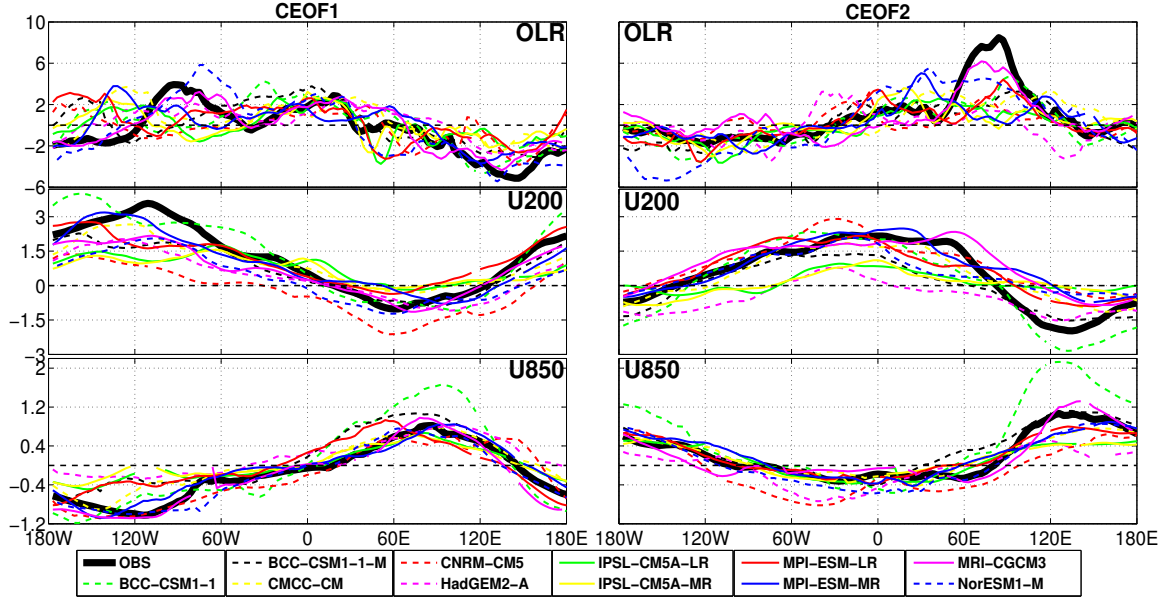


FIGURE 2 – Observed (thick black line) and simulated first two CEOFs of summer OLR and zonal wind at 850hPa and 200hPa anomalies from AMIP simulations. The first line of figures represent OLR, the second one the zonal wind at 200hPa and the last one the zonal wind at 850hPa anomalies. The units are W/m^2 per standard deviation of the associated first two CEOFs for OLR and m/s per standard deviation for zonal wind.

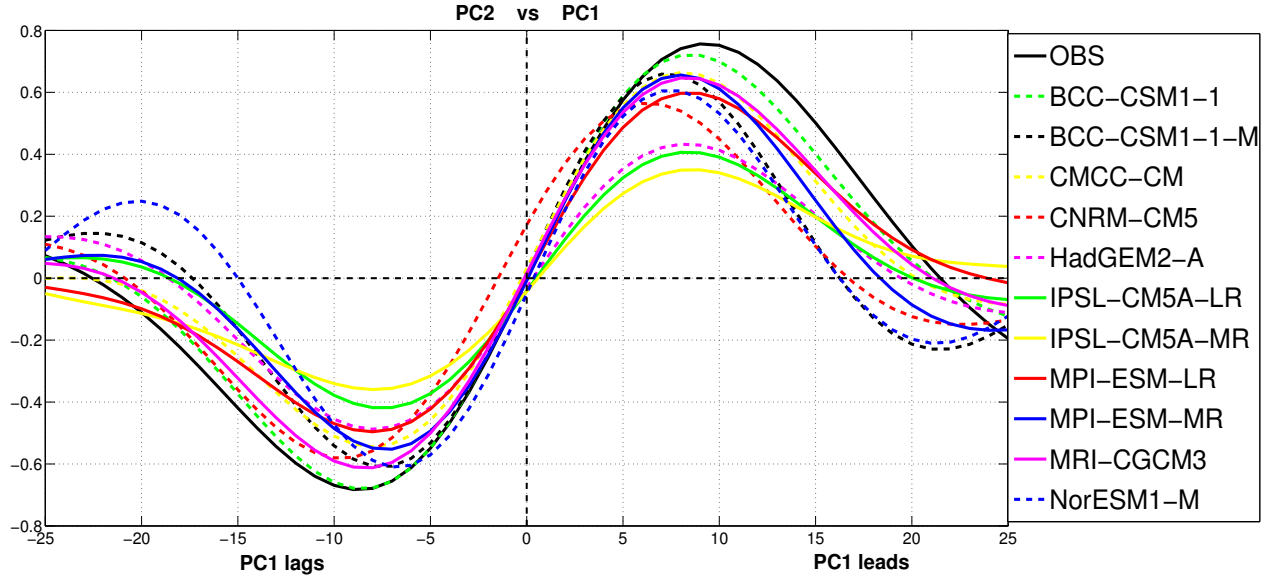


FIGURE 3 – Lead-lag correlations between the principal components associated with the first and second CEOF from observation and AMIP simulations. The x-axis of this figure is in days while the y-axis represents the lead-lag correlation coefficients between PC1 and PC2.

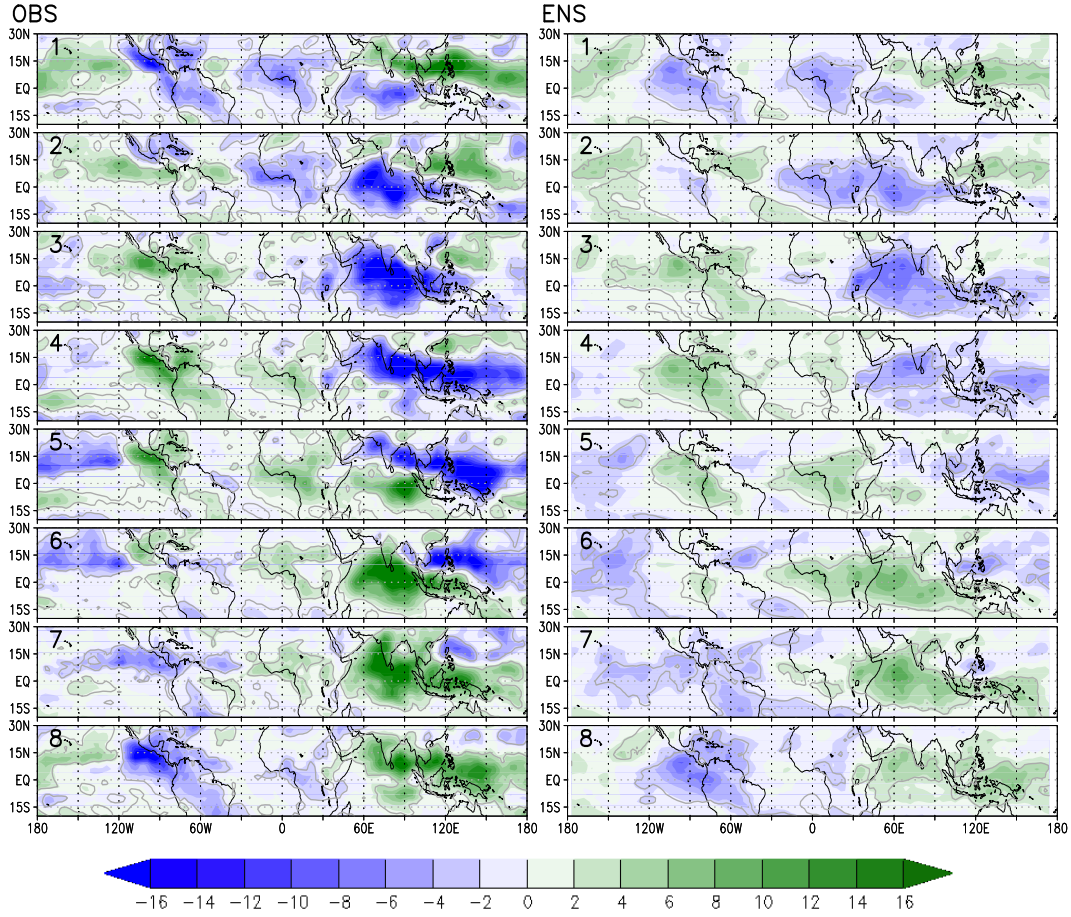


FIGURE 4 – Summer composites of deseasonalized anomalies of OLR according to the eight phases associated with the MJO, from observations (left) and the ensemble average of AMIP simulations (right). The units are W/m^2 . The grey contours represent the 95% significant regions obtained from a two-tailed t-test.

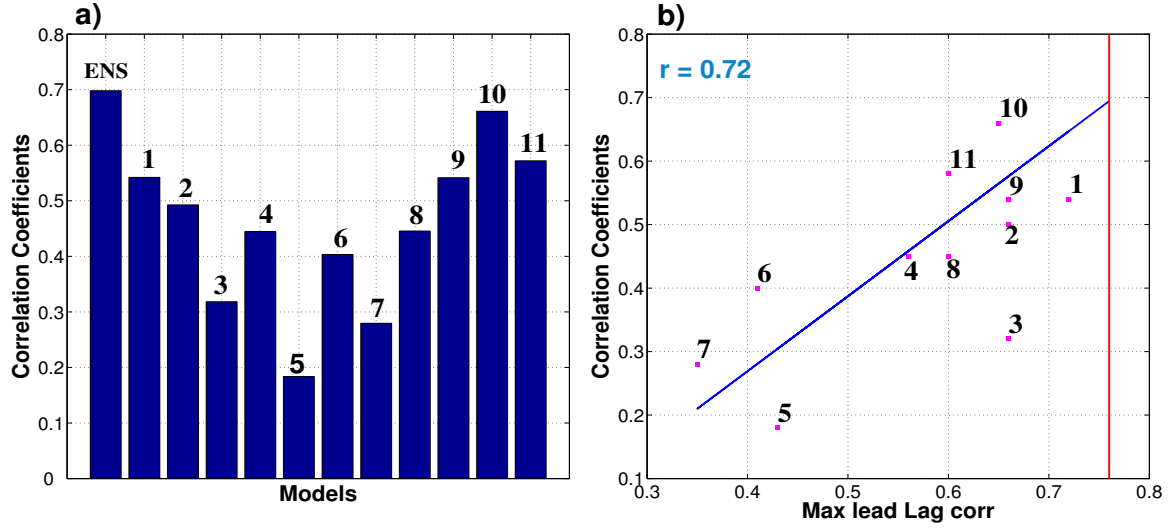


FIGURE 5 – a- Correlations of summer composites of deseasonalized OLR anomalies between the observations and AMIP simulations in the tropics (15°S-15°N). b- Scatterplot between the maximum lead lag correlation of the first two principal Components (PC1 and PC2) and the correlation coefficients between the observations and each of AMIP's models in the tropics presented in plot a). The red line in b) delimits the observed maximum lead lag correlation value. For convenience numbers are associated to the different models used through this study (see table 1).

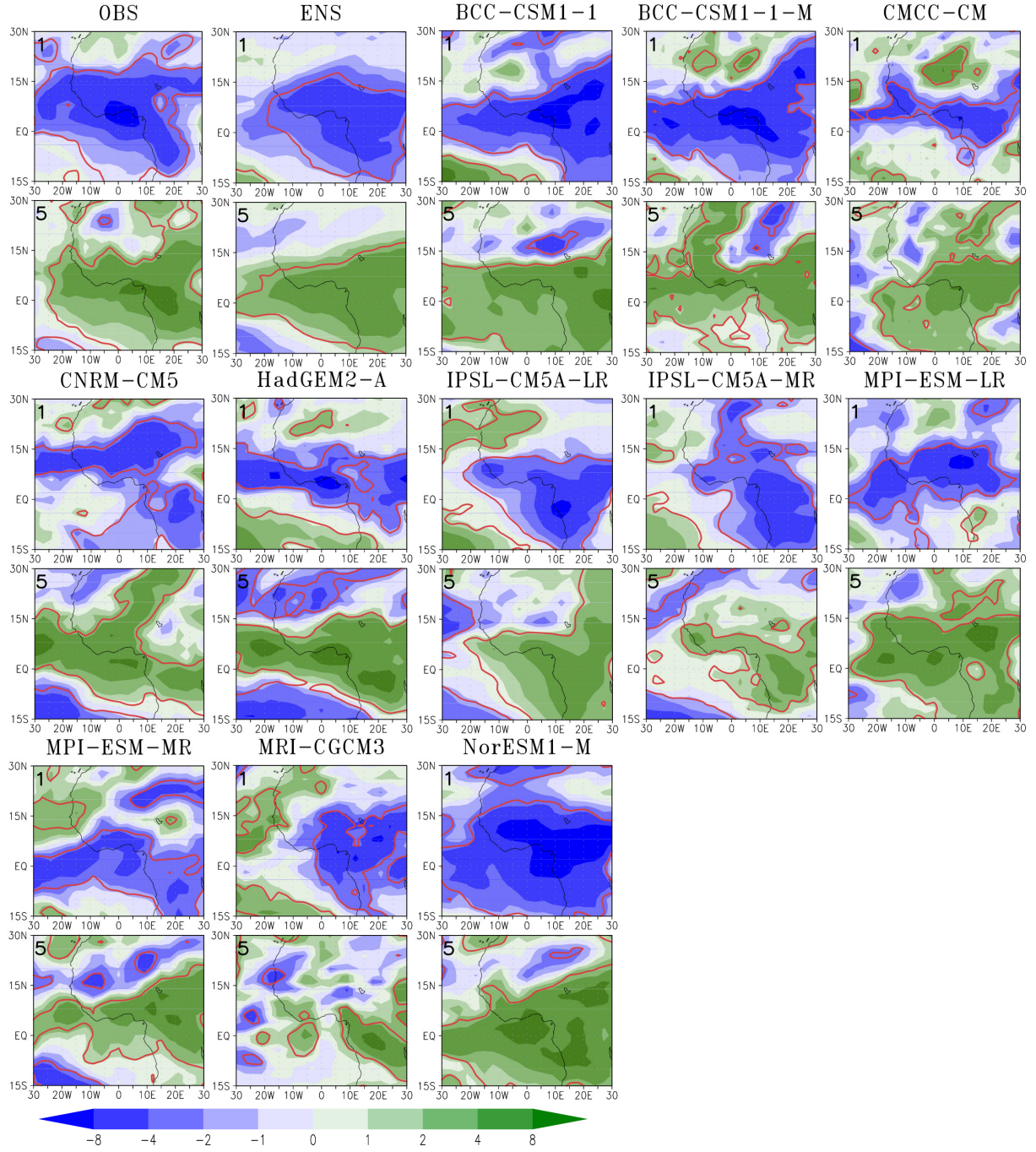


FIGURE 6 – Summer composites of observed deseasonalized anomalies of OLR (W/m^2) over West Africa during the strong (1) and weak (5) convective phases of MJO from the observations, individual AMIP simulations and the ensemble average of models. Red lines represent the 95% significant regions obtained from a two-tailed t-test.

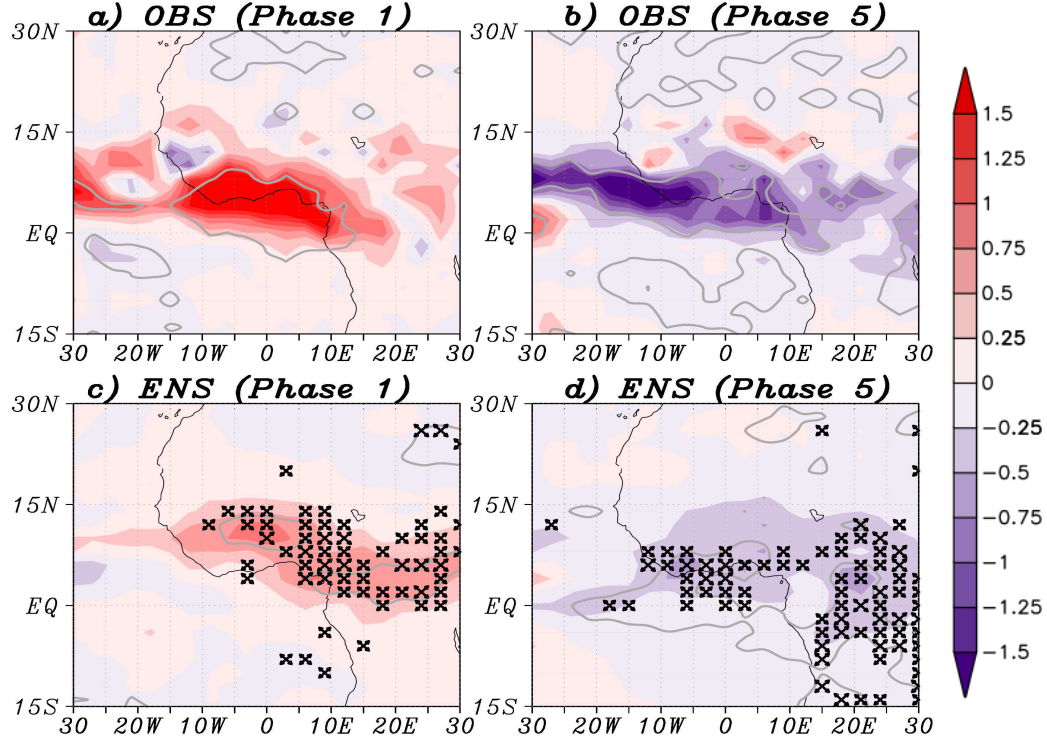


FIGURE 7 – Composites of rainfall anomalies (mm/day) during the MJO strong (a and c) and weak (b and d) convective phases over West Africa for the observations (a and b) and the ensemble average (c and d) of the models. The crosses mark the areas where at least eight (8) out of 11 models are consistent on the sign of the composite. Grey contours represent the area where rainfall anomalies are 95% significant according to a two-tailed t-test.

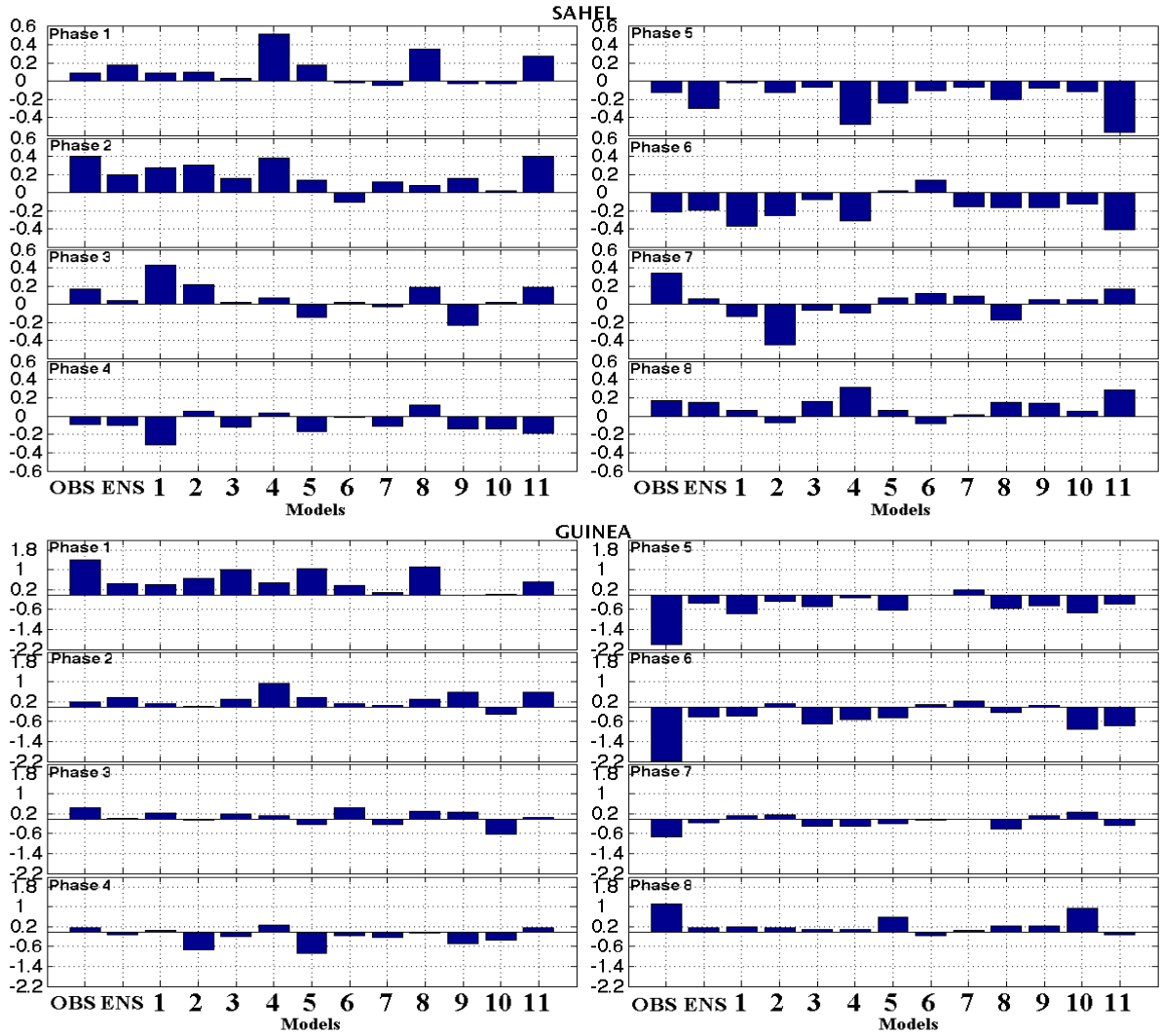


FIGURE 8 – Composites of observed and simulated deseasonalized rainfall (mm/day) anomalies averaged over the Sahel (20°W - 10°E and 10°N - 20°N) and Guinean Coast (12°W - 6°E and 4°N - 7°N) boxes for each phase in the observations, models and the ensemble average. The composites are averaged over the different boxes according to the different eight phases of MJO.

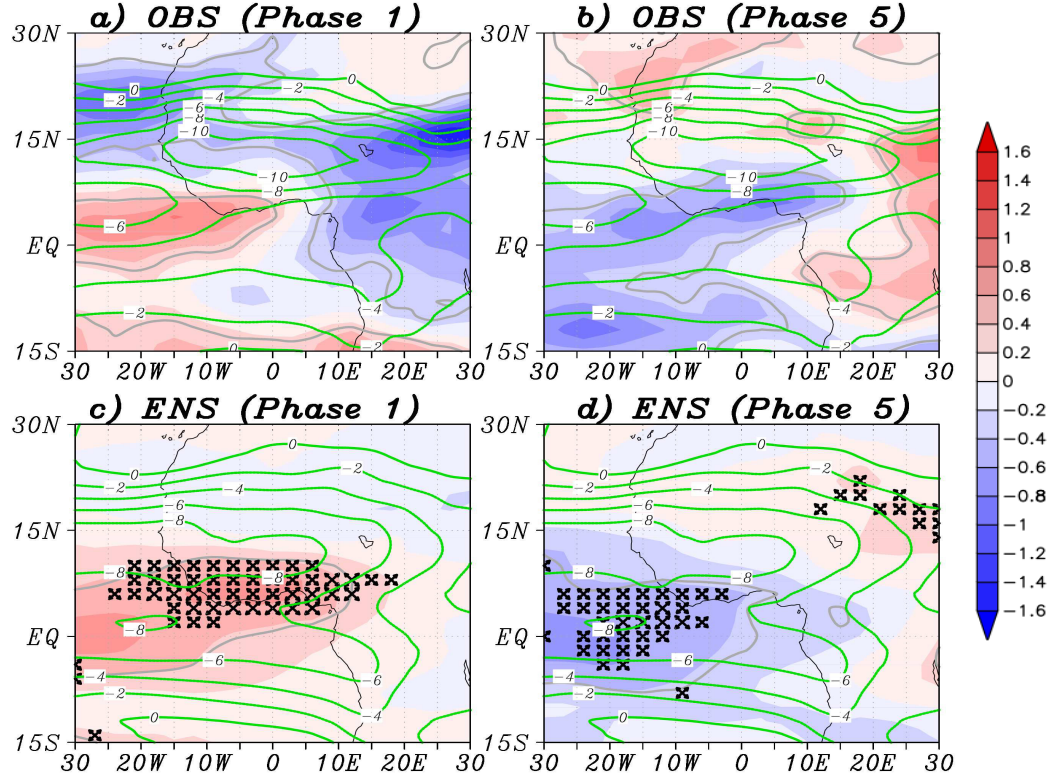


FIGURE 9 – Composites of zonal wind anomalies (m/s) at 600hPa (shaded) during the strong (a and c) and weak (b and d) convective phases of MJO from the observations (a and b) and the ensemble average of models (c and d) over West Africa. The green contour lines represent the climatological zonal wind at 600hPa. The crosses mark the areas where at least eight (8) out of 11 models are consistent on the sign of the composite. Grey contours represent the area where the zonal wind anomalies at 600hPa are 95% significant according to a two-tailed t-test.

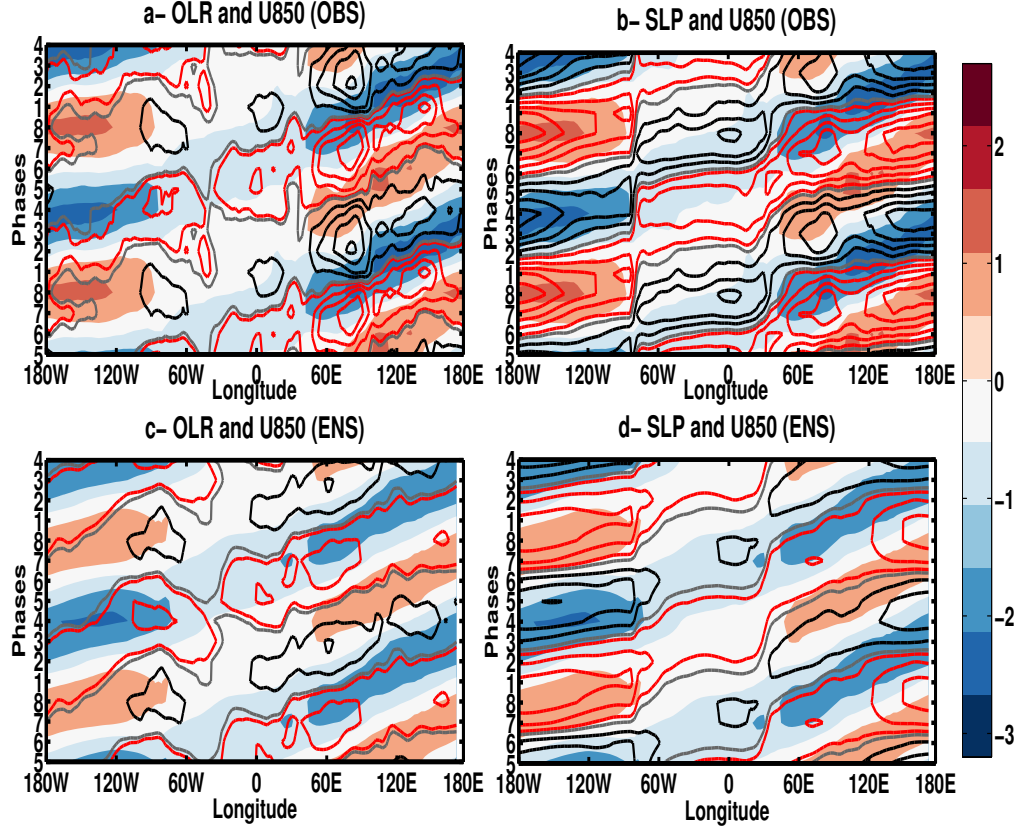


FIGURE 10 – Hovmoller diagram performed over the composite of deseasonalized anomalies averaged between 10°S and 10°N of zonal wind at 850hPa (m/s), OLR (W/m^2) and SLP (hPa) for observation (Fig. 10a and Fig. 10b) and simulations (Fig. 10c and Fig. 10d). Wind anomalies are shaded. The black solid contours represent the negative anomalous values of OLR (SLP) while the red solid contours highlight the positive ones in Fig. 10a and Fig. 10c (Fig. 10b and Fig. 10d). The grey lines represent the contour zero for OLR (Fig. 10a and Fig. 10c) and SLP (Fig. 10b and Fig. 10d). The OLR values vary from -16 to $16\text{W}/\text{m}^2$ while SLP's contours are ranging from -1 to 1hPa . The intervals between lines is $4\text{W}/\text{m}^2$ for OLR values and 0.2hPa for SLP's values.

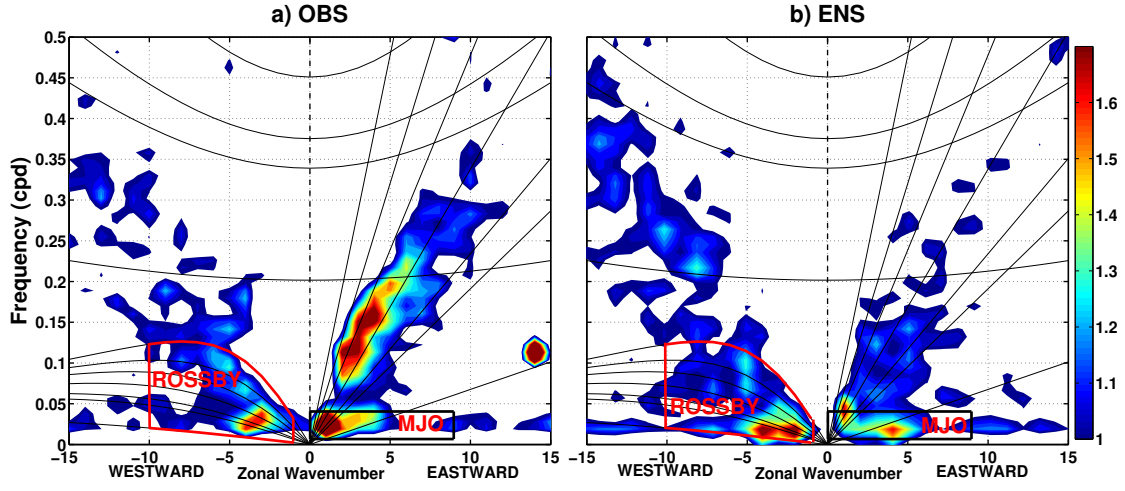


FIGURE 11 – Wavenumber frequency spectral analysis of OLR data from the observations (a) and the ensemble average of models (b). The eastward part of the signal (MJO) is extracted from 0 to 9 (see black box) of the periods of roughly 30-90 days and the westward part (corresponding to the Rossby waves) is extracted from -10 to 1 (see red box). The units are the ratio of the power spectra above the background OLR spectrum obtained after smoothing several times in wavenumber and in frequency.

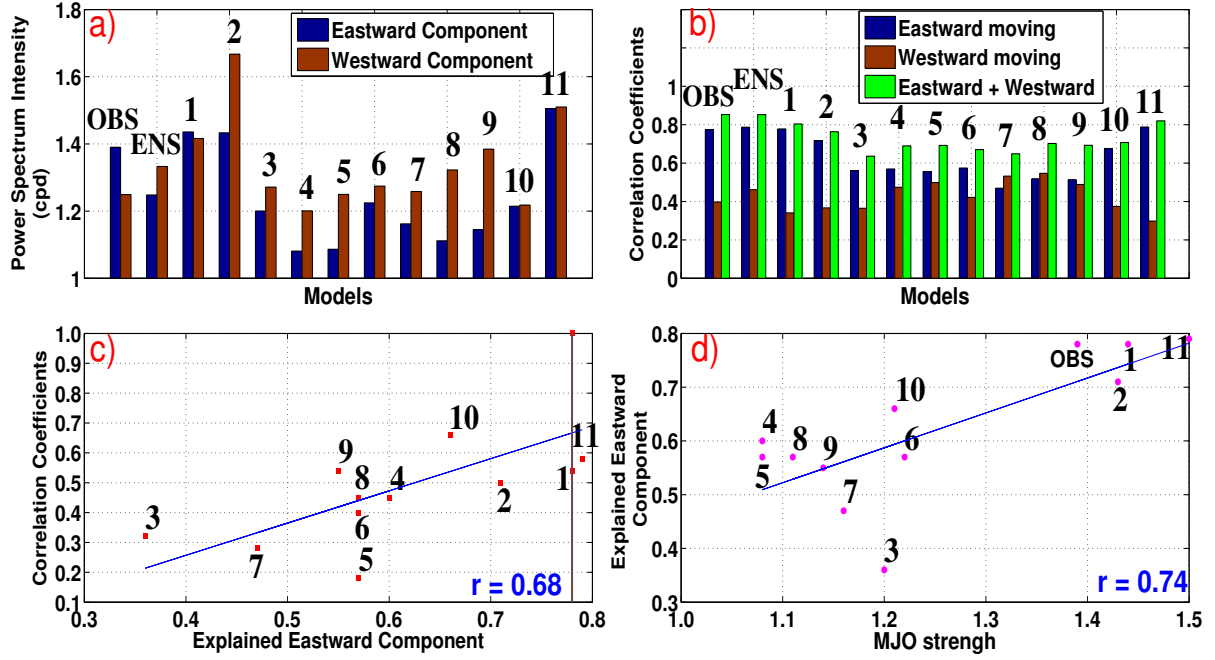


FIGURE 12 – a) Observed and simulated spectrum intensity above the background averaged over the different equatorial waves boxes (eastward and westward component) defined in figure 11. b) Spatial correlation in the tropics between MJO composites of unfiltered OLR and filtered OLR fields using the eastward and westward boxes defined in figure 11. c) Scatterplot between the correlation coefficients between the observations and each of AMIP’s models in the tropics and the composites of deseasonalized OLR filtered over MJO’s wavenumber-frequency box. The brown line in c delimits the observed value of the composites of deseasonalized OLR filtered over MJO’s wavenumber-frequency box. d) Scatterplot between the strength of MJO and the composites of deseasonalized OLR filtered over MJO’s wavenumber-frequency box.

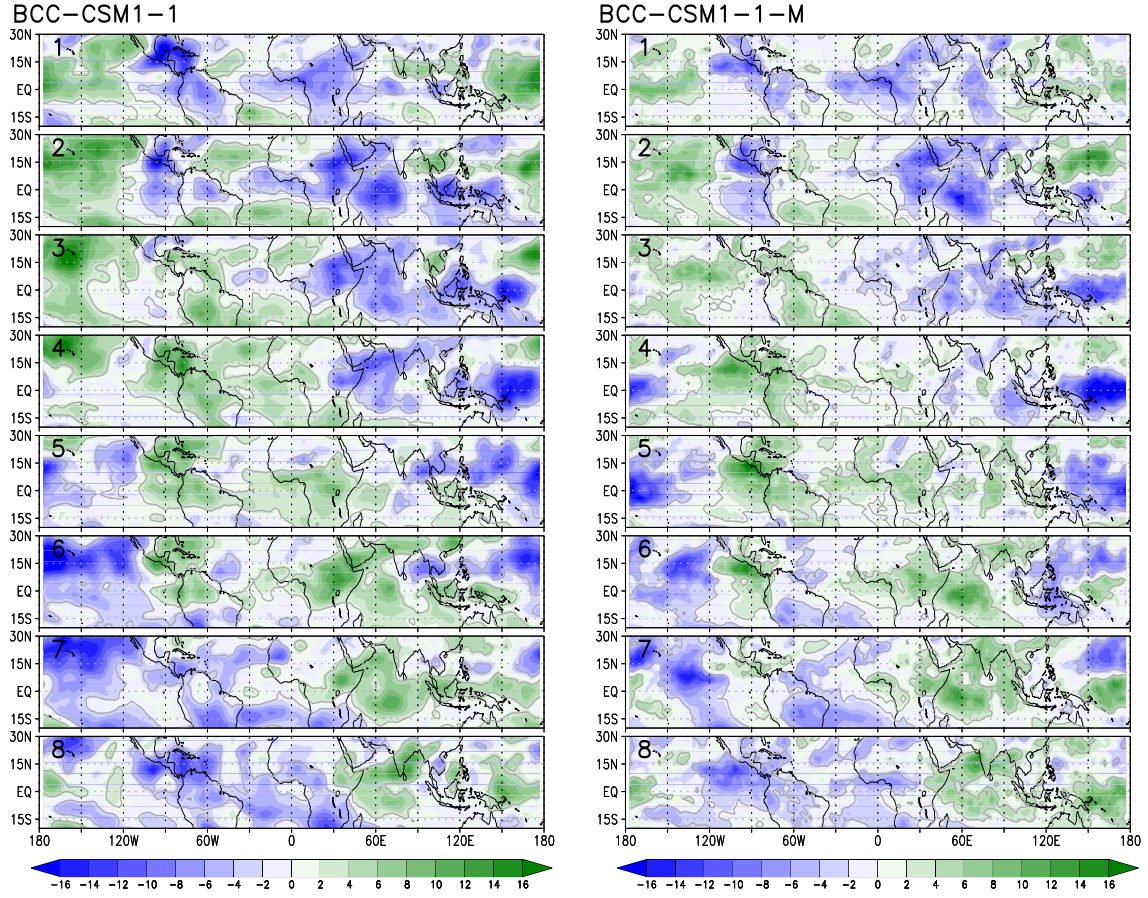


Figure S1 : Summer composites of deseasonalized anomalies of OLR according to the eight phases of MJO for BCC-CSM1-1 (left) and BCC-CSM1-1-M (right) models. The units are W/m^2 . The grey contours represent 95% significant regions obtained from a two-tailed t-test.

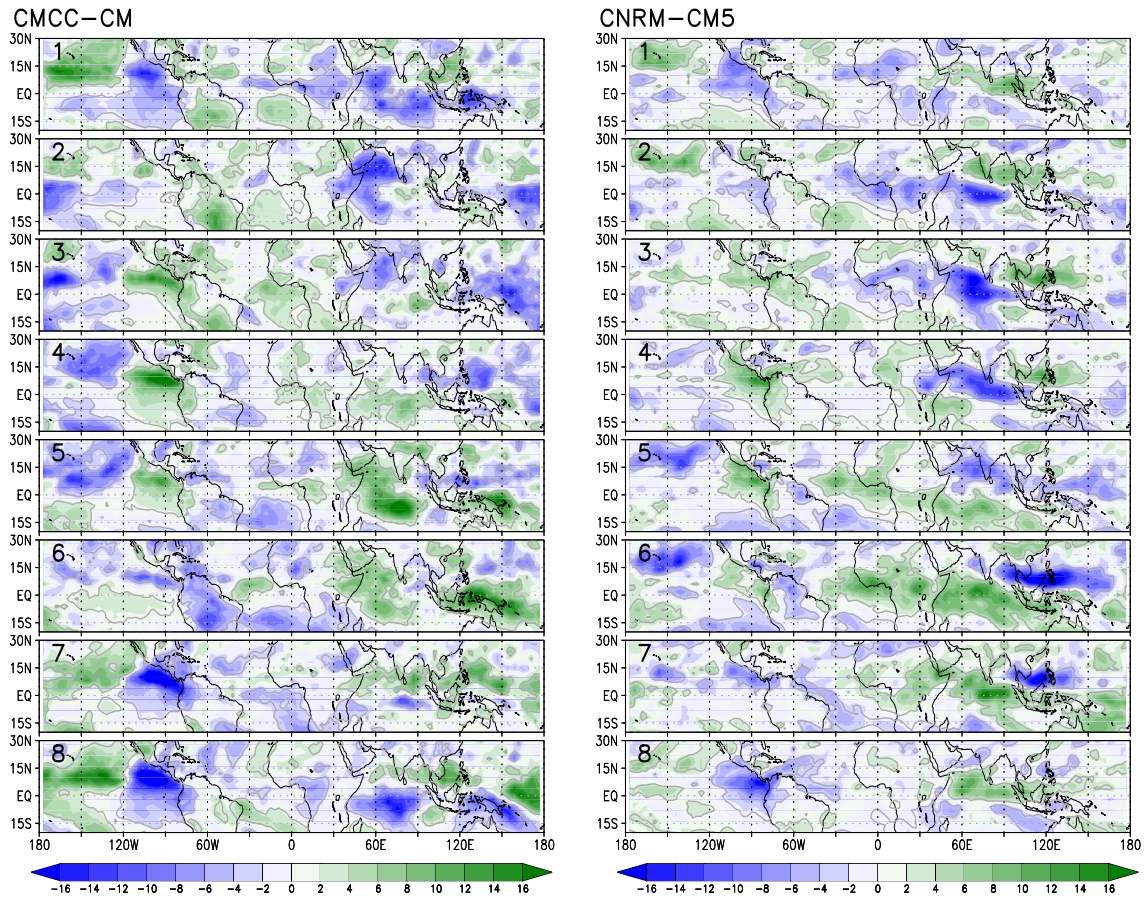


Figure S2 : Same as Fig. S1 for CMCC-CM (left) and CNRM-CM5 (right) models.

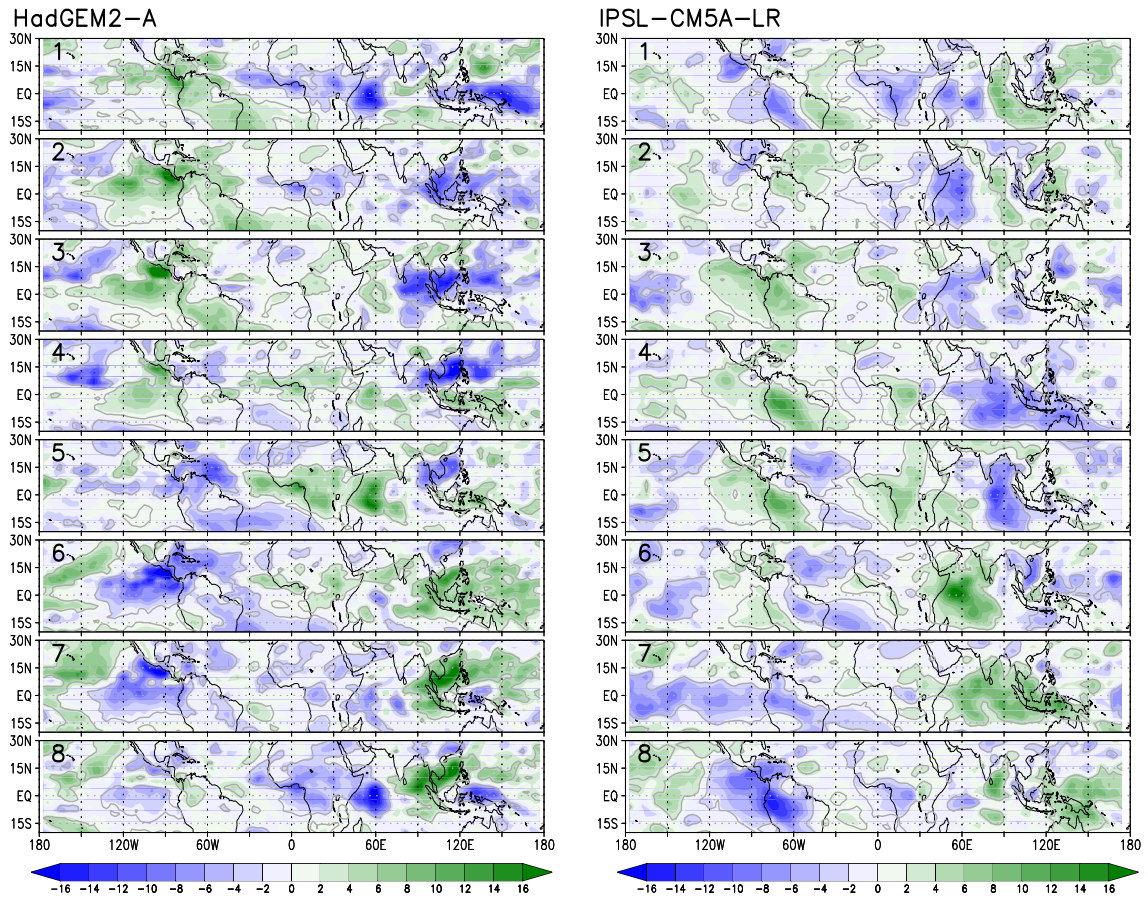


Figure S3 : Same as Fig. S1 for HadGEM2-A (left) and IPSL-CM5A-LR (right) models.

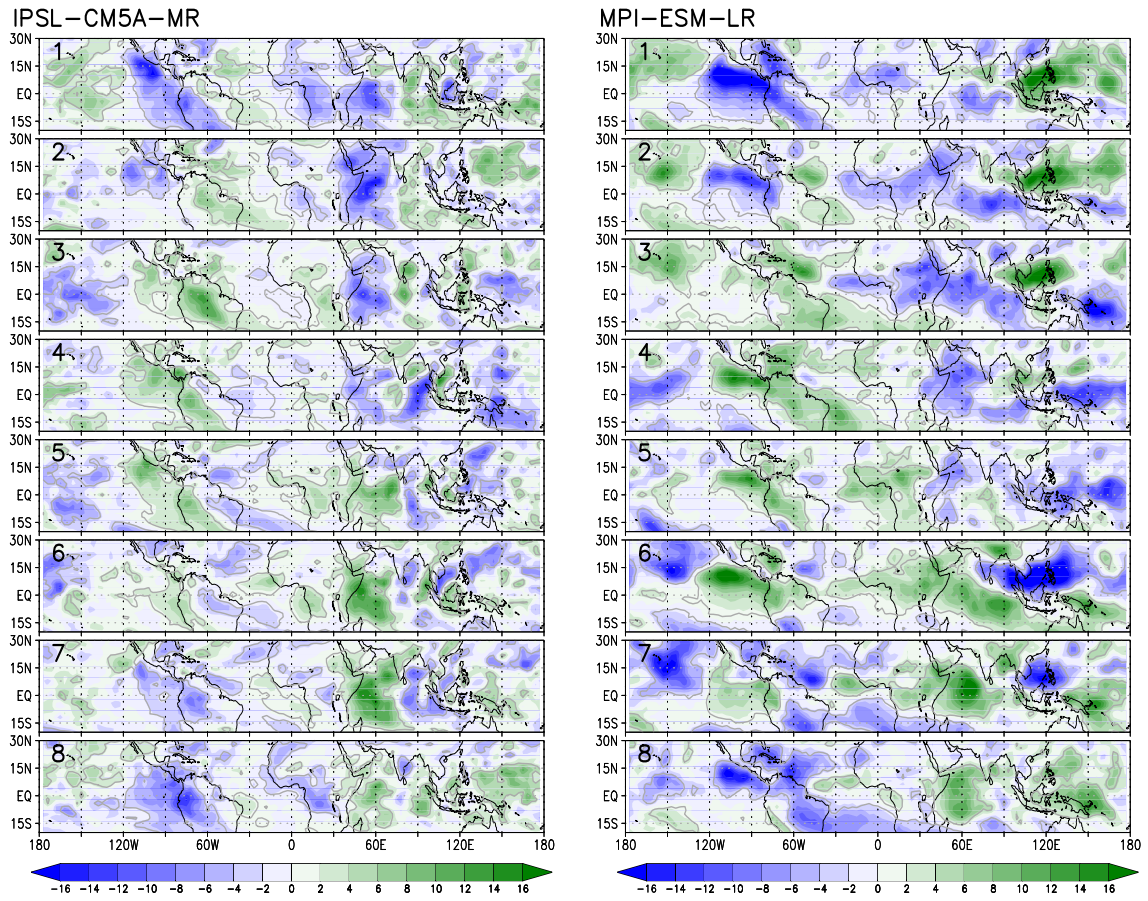


Figure S4 : Same as Fig. S1 for IPSL-CM5A-MR (left) and MPI-ESM-LR (right) models.

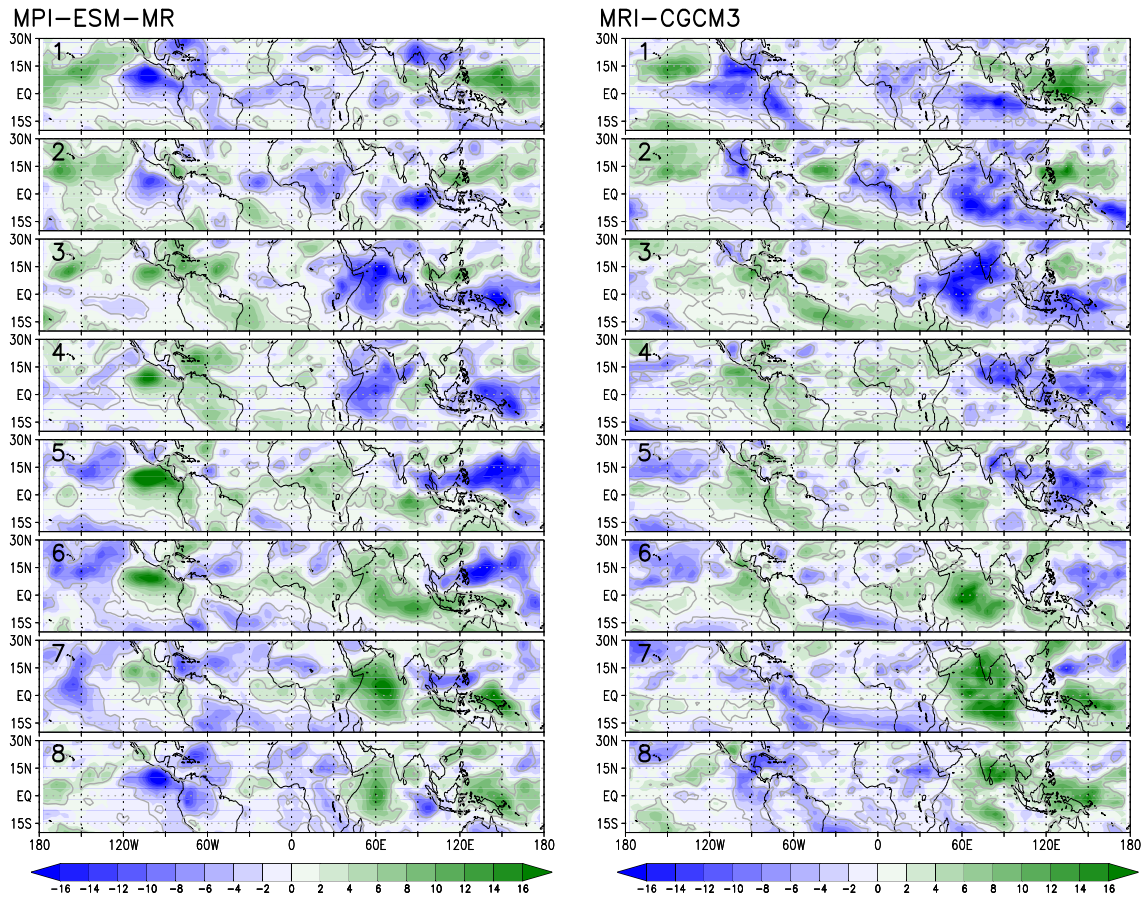


Figure S5 : Same as Fig. S1 for MPI-ESM-MR (left) and MRI-CGCM3 (right) models.

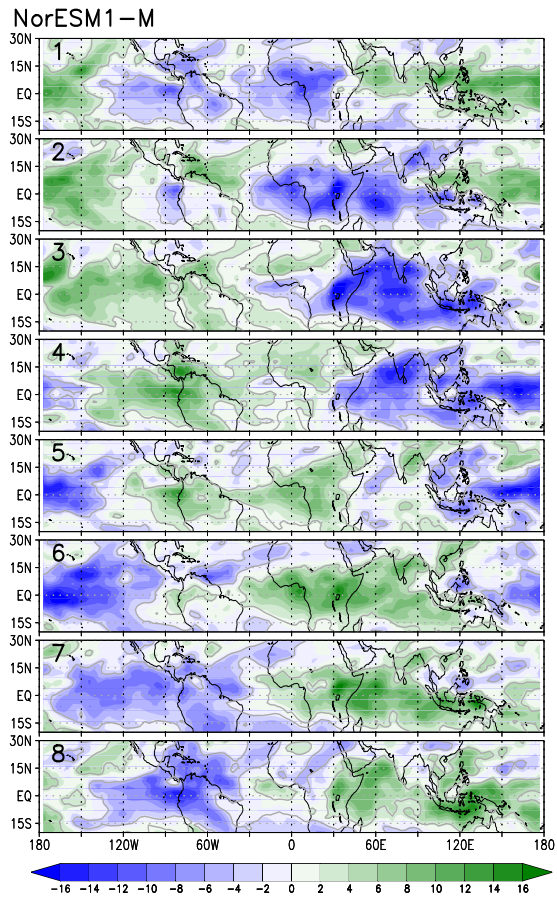


Figure S6 : Same as Fig. S1 for NorESM1-M model.

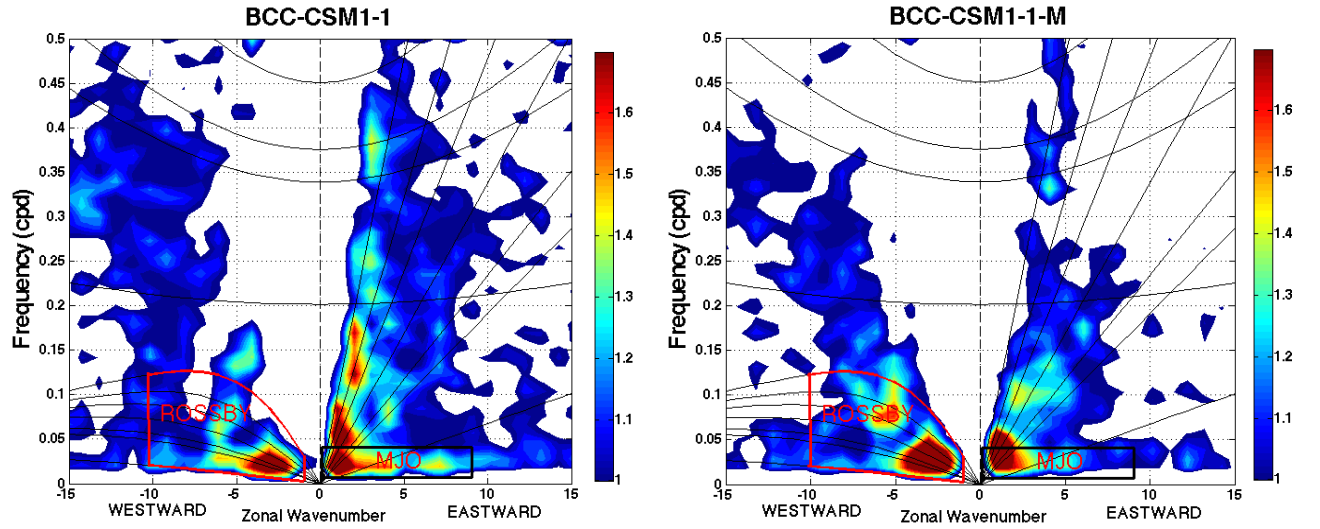


Figure S7 : Wavenumber frequency spectral analysis of OLR data for BCC-CSM1-1 (left) and BCC-CSM1-1-M (right) models. The eastward part of the signal (MJO) is extracted from 0 to 9 (see black box) of the periods of roughly 30-90 days and the westward part (corresponding to the Rossby waves) is extracted from -10 to 1 (see red box). The units are the ratio of the power spectra above the background OLR spectrum obtained after smoothing several times in wavenumber and in frequency.

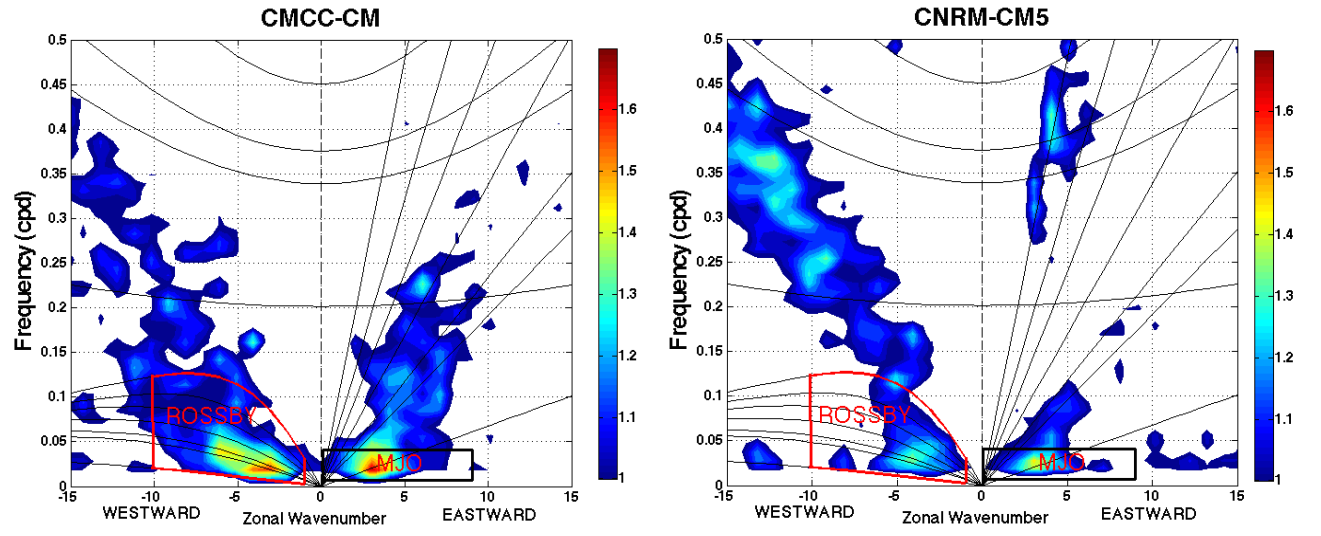


Figure S8 : Same as Fig. S7 for CMCC-CM (left) and CNRM-CM5 (right) models.

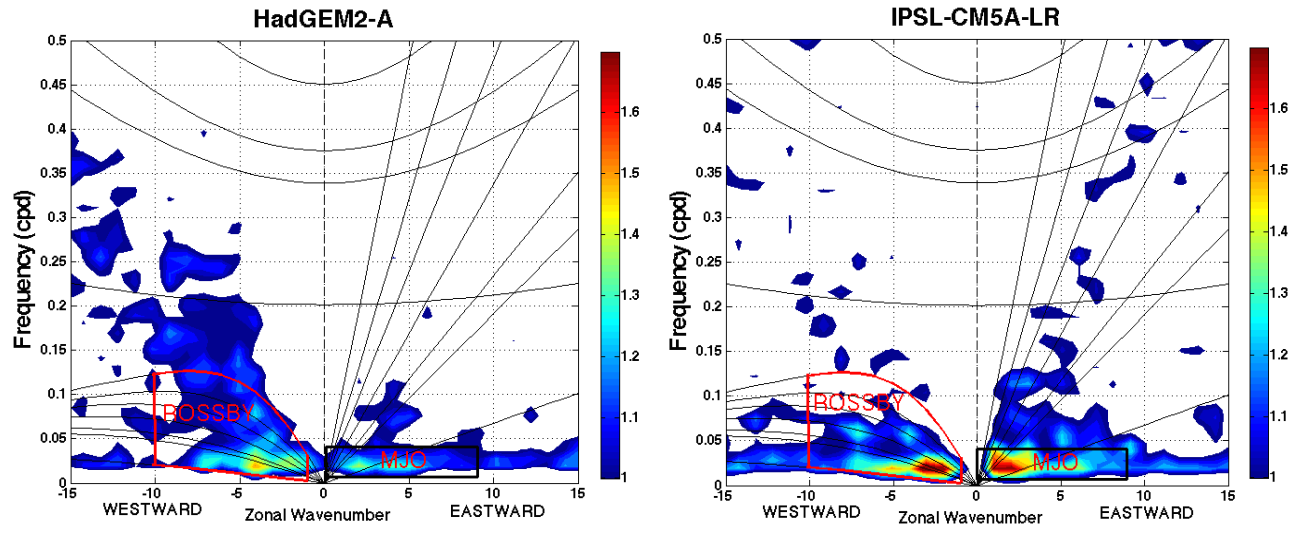


Figure S9 : Same as Fig. S7 for HadGEM2-A (left) and IPSL-CM5A-LR (right) models.

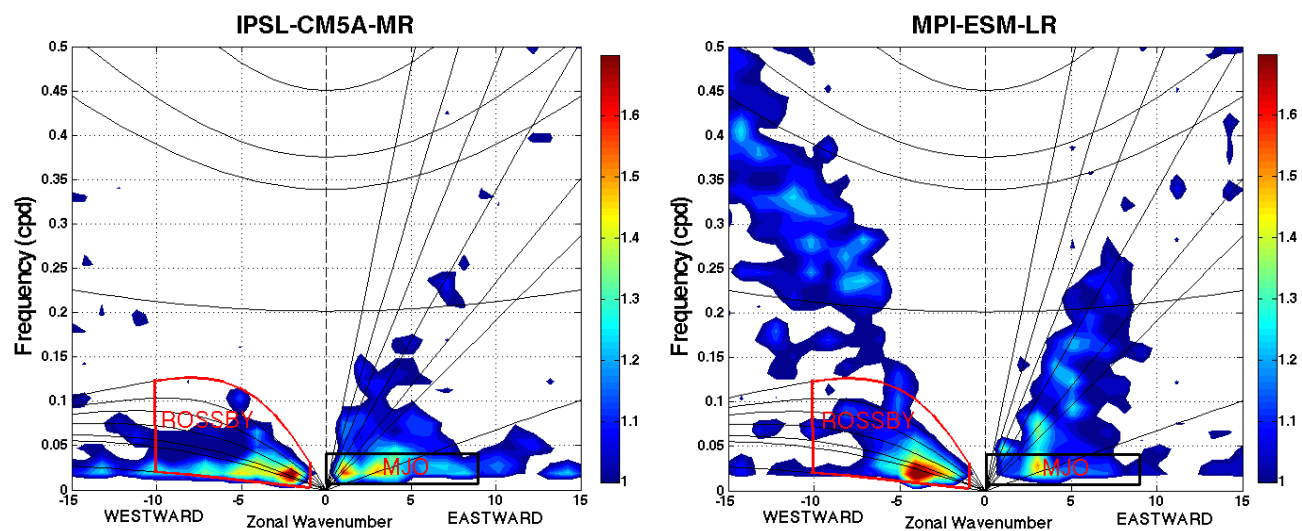


Figure S10 : Same as Fig. S7 for IPSL-CM5A-MR (left) and MPI-ESM-LR (right) models.

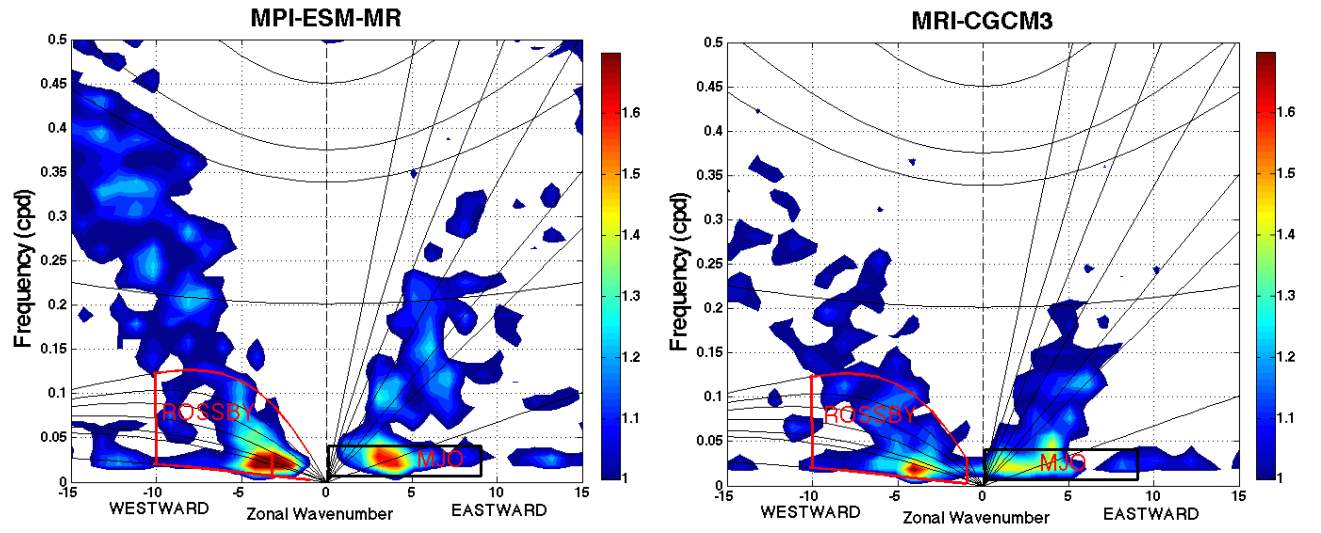


Figure S11 : Same as Fig. S7 for MPI-ESM-MR (left) and MRI-CGCM3 (right) models.

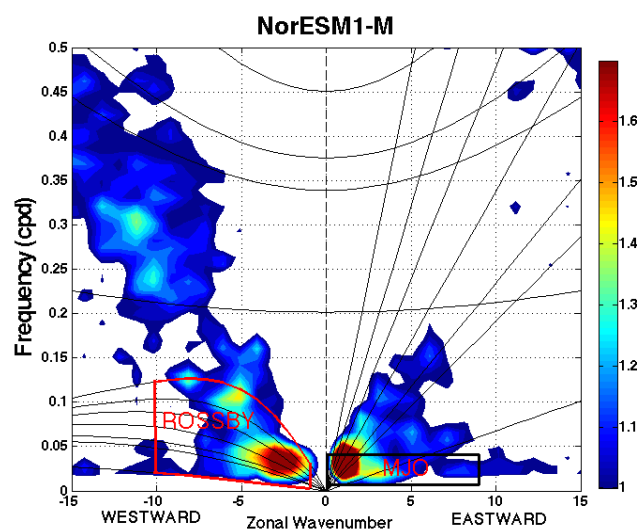


Figure S12 : Same as Fig. S7 for NorESM1-M model.